



## Article

# Ozone-Assisted Hydrothermal Synthesis Method of Sb-Doped SnO<sub>2</sub> Conductive Nanoparticles for Carbon-Free Oxygen-Reduction-Reaction Catalysts of Proton-Exchange-Membrane Hydrogen Fuel Cells

Takeshi Fukuda <sup>1</sup>, Kenji Iimura <sup>2</sup>, Takanori Yamamoto <sup>1</sup>, Ryuki Tsuji <sup>1</sup> , Maito Tanabe <sup>1</sup>, Seiji Nakashima <sup>3</sup> , Naoki Fukumuro <sup>2</sup>  and Seigo Ito <sup>1,\*</sup> 

<sup>1</sup> Department of Materials and Synchrotron Radiation Engineering, Graduate School of Engineering, University of Hyogo, 2167 Shosha, Himeji 671-2280, Hyogo, Japan; spurs20takeshi@gmail.com (T.F.); r2g128@gmail.com (R.T.)

<sup>2</sup> Department of Chemical Engineering and Materials Science, Graduate School of Engineering, University of Hyogo, 2167 Shosha, Himeji 671-2280, Hyogo, Japan; iimura@eng.u-hyogo.ac.jp (K.I.); fukumuro@eng.u-hyogo.ac.jp (N.F.)

<sup>3</sup> Department of Electronics and Computer Science, Graduate School of Engineering, University of Hyogo, 2167 Shosha, Himeji 671-2280, Hyogo, Japan; nakashima@eng.u-hyogo.ac.jp

\* Correspondence: itou@eng.u-hyogo.ac.jp; Tel./Fax: +81-79-267-4150



**Citation:** Fukuda, T.; Iimura, K.; Yamamoto, T.; Tsuji, R.; Tanabe, M.; Nakashima, S.; Fukumuro, N.; Ito, S. Ozone-Assisted Hydrothermal Synthesis Method of Sb-Doped SnO<sub>2</sub> Conductive Nanoparticles for Carbon-Free Oxygen-Reduction-Reaction Catalysts of Proton-Exchange-Membrane Hydrogen Fuel Cells. *Crystals* **2024**, *14*, 462. <https://doi.org/10.3390/cryst14050462>

Academic Editors: Mauro Francesco Sgroi and Sawanta S. Mali

Received: 7 June 2023

Revised: 9 May 2024

Accepted: 11 May 2024

Published: 15 May 2024

**Correction Statement:** This article has been republished with a minor change. The change does not affect the scientific content of the article and further details are available within the backmatter of the website version of this article.



**Copyright:** © 2024 by the authors. Licensee MDPI, Basel, Switzerland. This article is an open access article distributed under the terms and conditions of the Creative Commons Attribution (CC BY) license (<https://creativecommons.org/licenses/by/4.0/>).

**Abstract:** Proton-exchange-membrane hydrogen fuel cells (PEMFCs) are an important energy device for achieving a sustainable hydrogen society. Carbon-based catalysts used in PEMFCs' cathode can degrade significantly during operation-voltage shifts due to the carbon deterioration. The longer lifetime of the system is necessary for the further wide commercialization of PEMFCs. Therefore, carbon-free catalysts are required for PEMFCs. In this study, highly crystallized conducting Sb-doped SnO<sub>2</sub> (Sb-SnO<sub>2</sub>) nanoparticles (smaller than 7 nm in size) were synthesized using an ozone-assisted hydrothermal synthesis. Pt nanoparticles were loaded on Sb-SnO<sub>2</sub> supporting particles by polyol method to be "Pt/Sb-SnO<sub>2</sub> catalyst". The Pt/Sb-SnO<sub>2</sub> catalyst showed a high oxygen reduction reaction (ORR) mass activity (178.3 A g<sub>Pt</sub><sup>-1</sup> @ 0.9 V), compared to Pt/C (149.3 A g<sub>Pt</sub><sup>-1</sup> @ 0.9 V). In addition, the retention ratio from the initial value of electrochemical surface area (ECSA) during 100,000-voltage cycles tests between 1.0 V and 1.5 V, Pt/SnO<sub>2</sub> and Pt/Sb-SnO<sub>2</sub> catalyst exhibited higher stability (90% and 80%), respectively, than that of Pt/C catalyst (47%). Therefore, the SnO<sub>2</sub> and Sb-SnO<sub>2</sub> nanoparticles synthesized using this new ozone-assisted hydrothermal method are promising as carbon-free catalyst supports for PEMFCs.

**Keywords:** proton-exchange-membrane fuel cells; carbon-free catalysts; ozone-assisted hydrothermal method; antimony-doped tin oxide

## 1. Introduction

Proton-exchange-membrane hydrogen fuel cells (PEMFCs) are clean generator devices with multiple advantages, such as small size, lightweight, low noise, and high power density. They have been used as power sources for automobiles and stationary fuel cells. However, since the lifetime of PEMFCs for automotive applications is 2500–3000 h [1], the operation stability should be extended for further application. In PEMFCs, a Pt carbon (Pt/C) catalyst, which consists of platinum (Pt) nanoparticles supported on porous carbon, is used for the cathode. The carbon can be degraded with the voltage variation at the starting-up and shutting-down [2–7]. In addition, it has been reported that when a portion of the anode is exposed to air, the voltage at the cathode jumps up to 1.4–2.0 V [8–10]. Under such conditions, carbon is easily oxidized to CO<sub>2</sub>, resulting in the deterioration of

PEMFC performance. Hence, various studies have been conducted to develop materials that can be replaced with carbon.

In order to replace the carbon support, metal oxides have been studied intensively because they are chemically stable and conductive, such as titanium oxide (TiOx) [11], titanium carbide (TiC) [12], tungsten oxide (WOx) [13], iridium oxide (IrOx) [14], ruthenium oxide (RuOx) [14], cerium oxide (CeOx) [15], manganese oxide (MnOx) [16] and tin oxide (SnOx) [17–47]. Among these, SnO<sub>2</sub> is one of the most actively studied materials because it is very stable under the operating voltage of PEMFCs [23,25]. Moreover, it exhibits very high electrical conductivity when doped with other elements. For the dopants, antimony (Sb), niobium (Nb), and tantalum (Ta) are typical elements that have been reported as PEMFC catalyst supports and showed high activity and durability as Pt-supporting catalysts [17,19,21,22,24–27,32–47]. In addition, SnO<sub>2</sub> can be produced at a low cost. Moreover, SnO<sub>2</sub> is a transition metal-oxide semiconductor, and it is not only utilized in fuel cells but also in various devices such as solar cells [48], displays [49], and gas sensors [50].

There are multiple reports about synthesis methods of SnO<sub>2</sub> as Pt (or another catalyst) supports for PEMFCs: sol–gel (including precipitation) methods with annealing [17–27], polyol crystallization without annealing [28], hydrothermal synthesis with annealing [29] and without annealing [30,31], flame oxide-forming [32–44], electrospinning with annealing [45,46], and atomic layer deposition (ALD) [47]. There is also the problem of additives, such as surfactants, which can cause contamination. The organic additives can be eliminated by high-temperature annealing, resulting in the formation of a large and stable aggregation of SnO<sub>2</sub> nanoparticles.

To solve these problems, a method using ozone bubbling has been recently developed at the University of Hyogo, Japan [51]. This is a method that converts the precursors into SnO<sub>2</sub> nanoparticles using the strong oxidizing power of ozone. This method is quite useful because SnO<sub>2</sub> nanoparticles are synthesized reproducibly by very simple control without surfactant. Moreover, there is no report on synthesizing conductive SnO<sub>2</sub> nanoparticles by doping using this ozone method.

In this study, we developed a new method (ozone-assisted hydrothermal method) that combines an ozone-based synthesis followed by hydrothermal crystallization (without annealing). Using this new combination, well-crystallized Sb-doped SnO<sub>2</sub> (Sb-SnO<sub>2</sub>) nanoparticles were synthesized without surfactant and annealing procedure. The Sb doping ratios into SnO<sub>2</sub> for the PEMFC catalyst support were selected as 5 at.% and 10 at.%, according to previous publications [17,22,24–27,32,33,44,52,53]. For the application, these SnO<sub>2</sub> and Sb-doped SnO<sub>2</sub> (Sb-SnO<sub>2</sub>) nanoparticles prepared by the ozone-assisted hydrothermal method were synthesized, and their material and electrochemical properties were evaluated for cathode catalyst supports in PEMFCs.

## 2. Experiment

### 2.1. Materials

All chemicals were used as purchased, without further purification: tin(II) fluoride (SnF<sub>2</sub>, 90.0%, FUJIFILM Wako Pure Chemical Corporation, Osaka, Japan), antimony trichloride (SbCl<sub>3</sub>, FUJIFILM Wako Pure Chemical Corporation), 25% tetramethylammonium hydroxide solution ((CH<sub>3</sub>)<sub>4</sub>NOH, FUJIFILM Wako Pure Chemical Corporation), methanol (CH<sub>3</sub>OH, 99.8%, KANTO CHEMICAL Co., Inc., Tokyo, Japan), ethylene glycol (EG, HOCH<sub>2</sub>CH<sub>2</sub>OH, FUJIFILM Wako Pure Chemical Corporation), hydrogen hexachloroplatinate(IV) 6-hydrate, 98.5%, KISHIDA CHEMICAL Co., Ltd., Osaka, Japan), ethanol (C<sub>2</sub>H<sub>5</sub>OH, 99.5%, KANTO CHEMICAL Co., Inc.), 2-propanol ((CH<sub>3</sub>)<sub>2</sub>CHOH, 99.7%, KANTO CHEMICAL Co., Inc.), nafion<sup>®</sup> perfluorinated resin solution (5 wt.% in lower aliphatic alcohols and water, contains 15–20% water, Sigma-Aldrich Japan, Tokyo, Japan), perchloric acid 70% (HClO<sub>4</sub>, 70%, KISHIDA CHEMICAL Co., Ltd., Osaka, Japan), platinum carbon catalyst (46.8% Pt loading Pt/C, TEC10E50E, TANAKA Precious Metals., Tokyo, Japan).

## 2.2. Preparation Method of SnO<sub>2</sub> and Sb-SnO<sub>2</sub> Nanoparticles

The synthesis method is summarized in Figure 1. The amount of Sb (5 at.% and 10 at.%) in SnO<sub>2</sub> is the mixed ratio for the synthesis, not the resulting doped amount. The exact doped values were measured by XRF, shown in the Section 3. Figure 1 shows a block chart of the synthesis method for 5 at.% Sb-doped SnO<sub>2</sub>. A total of 0.784 g of tin fluoride (SnF<sub>2</sub>) in 10 mL H<sub>2</sub>O and 0.060 g of antimony chloride (SbCl<sub>3</sub>) in 37.5 mL H<sub>2</sub>O were mixed and stirred with a magnetic stirring bar until the solution became transparent (for 10 at.% doping, the amount of SbCl<sub>3</sub> was doubled to be 0.120 g). A solution of 4.3 mL of tetramethylammonium hydroxide (TMAH) was added and sonicated for 1 min, and the solution became milky white. Ozone bubbling was performed for 1 h using an ozone generator (OZONE WAVE, SYOKEN Corporation, Tokyo, Japan) with stirring at 850 rpm at 70 °C. The ozone flow rate was set at 3 L min<sup>-1</sup> (Lpm), and the applied power was 80% of the system. During the ozone bubbling, the milky-white solution gradually turns yellow and transparent. Using a rotary evaporator, the reacted solution was densified until the solution volume was reduced to 20 mL. The solution was transferred to a Teflon-internal-vessel and stainless-steel-out jacket autoclave (Model 4744, General Purpose Acid Digestion Vessel, 45 mL, Parr Instrument Company, Moline, IL, USA) and placed in an electric furnace at 240 °C for 12 h. The dark blue precipitate was obtained by centrifugation. The precipitate was dispersed in H<sub>2</sub>O and centrifuged to remove the supernatant liquid with impurities 3 times. And then, the precipitation was dispersed in methanol using an ultrasonic homogenizer. Finally, the solution was transferred to a Petri dish and dried on a hot plate at 60 °C to be named “ozone-hydrothermal Sb-SnO<sub>2</sub>”. Each 10 at.% Sb-SnO<sub>2</sub> was synthesized by changing the amount of SbCl<sub>3</sub>. Each pure SnO<sub>2</sub> (without Sb dopant) was prepared in the same way without SbCl<sub>3</sub>.

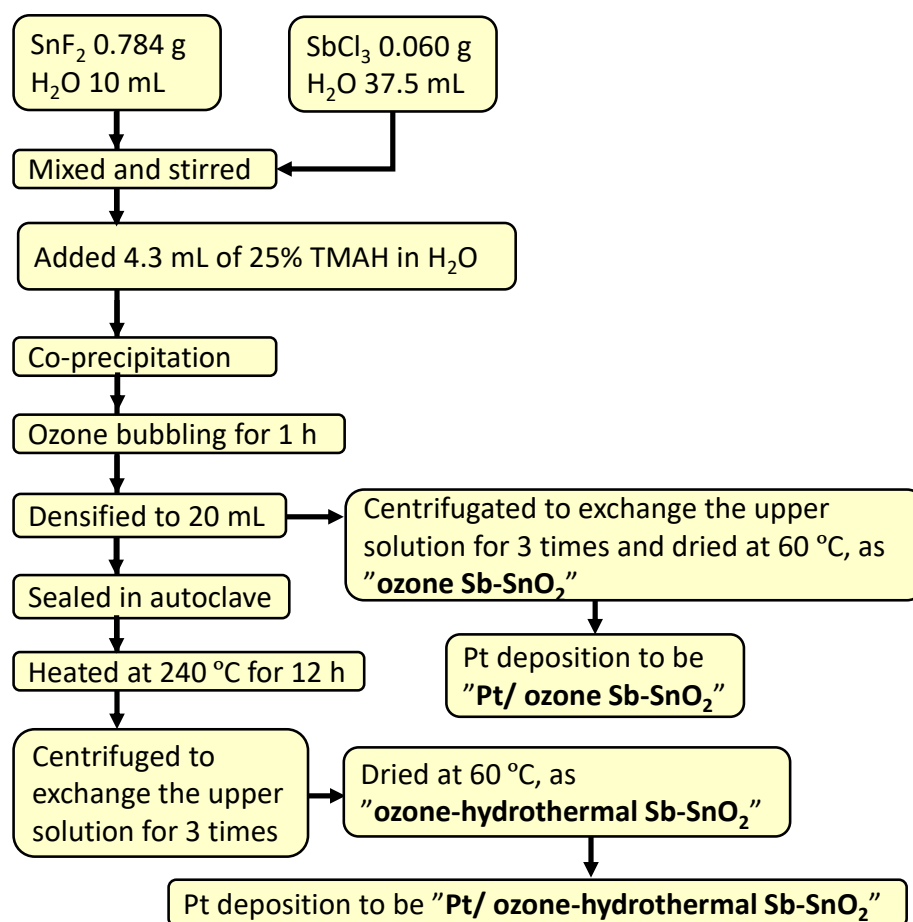


Figure 1. Synthesis method of Pt-deposited Sb-SnO<sub>2</sub> nanoparticles.

### 2.3. Preparation Method of Thin Films of $\text{SnO}_2$ and $\text{Sb-SnO}_2$

To evaluate conductivity, absorption spectra, and XRD patterns,  $\text{SnO}_2$ , 5 at.%  $\text{Sb-SnO}_2$ , and 10 at.%  $\text{Sb-SnO}_2$  thin films were prepared by spin-coating on glass substrates. Glass substrates were  $25 \times 25$  mm in size. Substrates were ultrasonically cleaned with ethanol and distilled water for 30 min, and then surface organics were removed with UV- $\text{O}_3$  cleaner (Tabletop UV/Ozone Processor, SEN LIGHTS Corporation, Osaka, Japan). Methanol was used as the solvent of  $\text{Sb-SnO}_2$  dispersion. It was thoroughly dispersed using an ultrasonic homogenizer. The concentration of the solution was 30 wt.%. A total of 120  $\mu\text{L}$  of the solution was dropped onto the glass substrate using a micropipette and spun at 2500 rpm for 20 s. To increase the thickness, the spin coating was repeated four times. Finally, the substrate was annealed at 450  $^\circ\text{C}$  for 2 h.

### 2.4. Preparation Method of $\text{Pt/SnO}_2$ and $\text{Pt/5 at.% Sb-SnO}_2$

Pt catalyst nanoparticles were prepared using a polyol method, as reported elsewhere [54]. As a platinum precursor solution, 1 g hexachloroplatinic acid hexahydrate was dissolved in 50 mL ethanol. A total of 81 mg of  $\text{Sb-SnO}_2$  powder was placed in a flask and mixed with 135 mL of EG/water (2:1) mixture at room temperature. While the solution was stirred with a magnetic stirring bar at room temperature, 2.69 mL of the platinum precursor solution was added. After sonication, the mixture was stirred for 12 h at room temperature. It was transferred to an oil bath and heated at 125  $^\circ\text{C}$  for 2 h with stirring to reduce platinum. The reactants were centrifuged with distilled water and dried in an oven at 60  $^\circ\text{C}$  overnight to be the  $\text{Pt/5 at.% Sb-SnO}_2$  powder. The targeting Pt amount at the synthesis was 20 wt%, and the XRF measured Pt amount was ca. 17 wt% in  $\text{Pt/5 at.% Sb-SnO}_2$ .  $\text{Pt/SnO}_2$  was prepared in the same way as above. In order to confirm the merit of the ozone-assisted hydrothermal method, a catalyst without the hydrothermal method (named “ $\text{Pt/ozone Sb-SnO}_2$ ” in Figure 1) was prepared and compared. The “ $\text{ozone Sb-SnO}_2$ ” was the colloidal nanoparticle after ozone bubbling in Figure 1, which was obtained by centrifugation and 60  $^\circ\text{C}$  drying.

### 2.5. Materials Characterizations

The atomic ratio of Sn/Sb in prepared  $\text{Sb-SnO}_2$  was measured by X-ray fluorescence (XRF, XGT-1000WR, HORIBA, Ltd., Kyoto, Japan). The crystal structure of  $\text{Sb-SnO}_2$  powder was evaluated by X-ray diffraction (XRD, MiniFlexII, Rigaku, Tokyo, Japan). The morphologies of  $(\text{Sb-})\text{SnO}_2$  and  $\text{Pt}/(\text{Sb-})\text{SnO}_2$  were observed by transmission electron microscope and high-angle annular dark field scanning transmission electron microscope (TEM and HAADF-STEM, Talos F200i, Thermo Fisher Scientific Japanese Group, Tokyo, Japan). The average crystallite size was calculated using the Scherrer's equation. The average nanoparticle size of  $\text{SnO}_2$  and  $\text{Sb-SnO}_2$  was evaluated using the TEM images. The aggregation size of nanoparticles dispersed in methanol was measured using dynamic light scattering (DLS, nanoSAQLA, Otsuka Electronics Co., Ltd., Osaka, Japan). X-ray photoelectron spectroscopy (XPS, PHI5000, ULVAC-PHI, Inc., Chigasaki, Japan) was performed to evaluate the constituent elements of the obtained  $\text{SnO}_2$  and  $\text{Sb-SnO}_2$ . The optical absorbance of thin films was evaluated by a UV/vis spectrometer (LAMBDA 750 UV/VIS Spectrometer, PerkinElmer Japan, Yokohama, Japan). The sheet resistance of thin films was measured using a resistivity meter (Lonerta-EP MCP-T360, Mitsubishi Chemical Corporation, Tokyo, Japan). Film thickness was measured using a scanning electron microscope (SEM, JSM-6510, JEOL, Tokyo, Japan). Conductivity was calculated from the obtained sheet resistance and film thickness.

### 2.6. Electrochemical Characterization of $\text{Pt/SnO}_2$ and $\text{Pt/Sb-SnO}_2$

Electrochemical measurements and catalyst evaluation were performed based on the reported method [43]. Electrochemical measurements were performed at room temperature using a rotating disk electrode system (RDE, HR-500, Meiden Hokuto Corporation, Tokyo, Japan) and a three-electrode cell. A reference electrode (reverse hydrogen electrode, RHE),

a working electrode (glassy carbon disk electrode, electrode surface area  $0.196 \text{ cm}^2$ ), a counter electrode (platinum wire electrode), and an electrolyte solution ( $0.1 \text{ M HClO}_4$ ) were used. Catalyst ink was prepared by mixing  $12 \text{ mg}$  of Pt/(Sb-)SnO<sub>2</sub>,  $5358 \text{ }\mu\text{L}$  of distilled water,  $1692 \text{ }\mu\text{L}$  of isopropanol, and  $28.2 \text{ }\mu\text{L}$  of 5% Nafion dispersion followed by sonication for 2 min using an ultrasonic homogenizer. A total of  $10 \text{ }\mu\text{L}$  of catalyst ink was applied on the surface of the glassy carbon disk electrode using a micropipette. And then, it dried in an oven at  $60 \text{ }^\circ\text{C}$  for 20 min. The amount of Pt loaded on the electrode was  $17.3 \text{ }\mu\text{g-Pt cm}^{-2}$ . For cyclic voltammetry (CV) and linear sweep voltammetry (LSV) measurements, a potentiostat (HZ-7000, Hokuto Denko Corporation, Tokyo, Japan) was used.

For the electrochemical surface area (ECSA), CV measurements were performed by sweeping the potential between  $0.05 \text{ V}$  and  $1.2 \text{ V}$  at  $50 \text{ mV s}^{-1}$  in  $\text{HClO}_4$  without rotating WE. Before the measurement,  $\text{N}_2$  gas was bubbled in the solution for 10 min. After 50 cycles of voltage sweeping and the confirmation of no variational result, the CV data were acquired. ECSA was determined by integrating the area of the hydrogen adsorption region ( $0.4\text{--}0.05 \text{ V}$ ) at the 50th cycle of CV voltammograms. Following the former research, the hydrogen adsorption electric capacitance per unit area of Pt was decided to be  $0.21 \text{ mC cm}^{-2}$  [55].

To evaluate the oxygen reduction reaction (ORR) activity, the mass activity (MA) of the catalyst was evaluated by liner-sweep voltammetry (LSV) measurements performed while rotating WE. LSV was recorded by sweeping a potential range of  $0.05$  to  $1.2 \text{ V}$  at a scan rate of  $10 \text{ mV s}^{-1}$ . Before the measurement,  $\text{O}_2$  gas was bubbled in the solution for 30 min. The rotational speeds of the working electrode were 100, 400, 900, 1600, and 2500 rpm. The Koutecky–Levich equation was applied to calculate the mass activity (MA) at  $0.9 \text{ V}$  vs. RHE.

The catalyst durability of ECSA was evaluated using a start-stop protocol (10,000 cycles of voltage sweeping with  $0.5 \text{ V s}^{-1}$  from  $1.0$  to  $1.5 \text{ V}$ ) to check the durability of supporting material (carbon or SnO<sub>2</sub>) [7] and a load cycle protocol (10,000 cycles of voltage steps kept at  $1.0 \text{ V}$  for 3 s and at  $0.6 \text{ V}$  for 3 s, alternatively) to check the durability of Pt nanoparticles on the supporting material [7]. Before the durability test, the LSV measurements were performed under oxygen saturation, and then, for the stability test,  $\text{N}_2$  gas was bubbled in the electrolyte solution for 20 min, and the initial ECSA data were measured by CV. To determine the retention rate of ECSA, the 5 cycles of CV measurements were measured after every 1000 cycles. The ECSA data were acquired at the 5th cycle of CV.

### 3. Result and Discussion

#### 3.1. Material Characteristics of SnO<sub>2</sub> and Sb-SnO<sub>2</sub>

To confirm the concentration of doped antimony, XRF measurements were performed on the Sb-SnO<sub>2</sub> powders (Table 1). The 5 at.% Sb-SnO<sub>2</sub> shows that the Sb/Sn ratio at the synthesis was kept in the resulting SnO<sub>2</sub> powder. In contrast, the 10 at.% Sb-SnO<sub>2</sub> had only 8 at.% Sb, and not all Sb ions are present in the SnO<sub>2</sub> lattice, which will be due to the limitation of doping amounts. Although 10 at.% of Sb doping was not in the SnO<sub>2</sub> lattice, this sample will continue to be referred to as “10 at.% Sb-SnO<sub>2</sub>” in this study. The detailed research of another concentration will be discussed in a future paper.

**Table 1.** Sn/Sb atomic ratio measured by XRF.

Sample	Sn/Sb Ratio/at.%	
	Sn	Sb
5 at.% Sb-SnO <sub>2</sub>	95.0	5.01
10 at.% Sb-SnO <sub>2</sub>	92.1	7.94

Figure 2a shows XRD measurements of SnO<sub>2</sub> powders synthesized by ozone-assisted process [51] and ozone-assisted hydrothermal process (this work). In order to express the crystallinity, the  $y$ -axis of Figure 2a shows the measured-XRD raw data, which are not the arbitrary unit (a.u.) because the arbitrary unit (a.u.) cannot be compared about the

largeness of the  $y$ -axis. As a result of the hydrothermal treatment, the crystalline of  $\text{SnO}_2$  was significantly improved compared to only the ozone-assisted process. Figure 2b shows XRD measurements of  $\text{Sb-SnO}_2$  powders with different antimony synthesis concentrations. Peaks showed tetragonal rutile structure derived from  $\text{SnO}_2$  in all  $\text{Sb-SnO}_2$  at 0, 5, and 10 at.%. In addition, no additional peaks by Sb doping appeared (such as  $\text{Sb}_2\text{O}_3$ ). Figure 2c shows a magnified view of the (101) peak of  $\text{Sb-SnO}_2$ . A slight shift of the peak position to a lower angle was observed with increasing Sb doping concentration, resulting in the  $\text{SnO}_2$  lattice expansion. Therefore, it can be concluded that Sb was doped in the  $\text{SnO}_2$  lattice effectively.

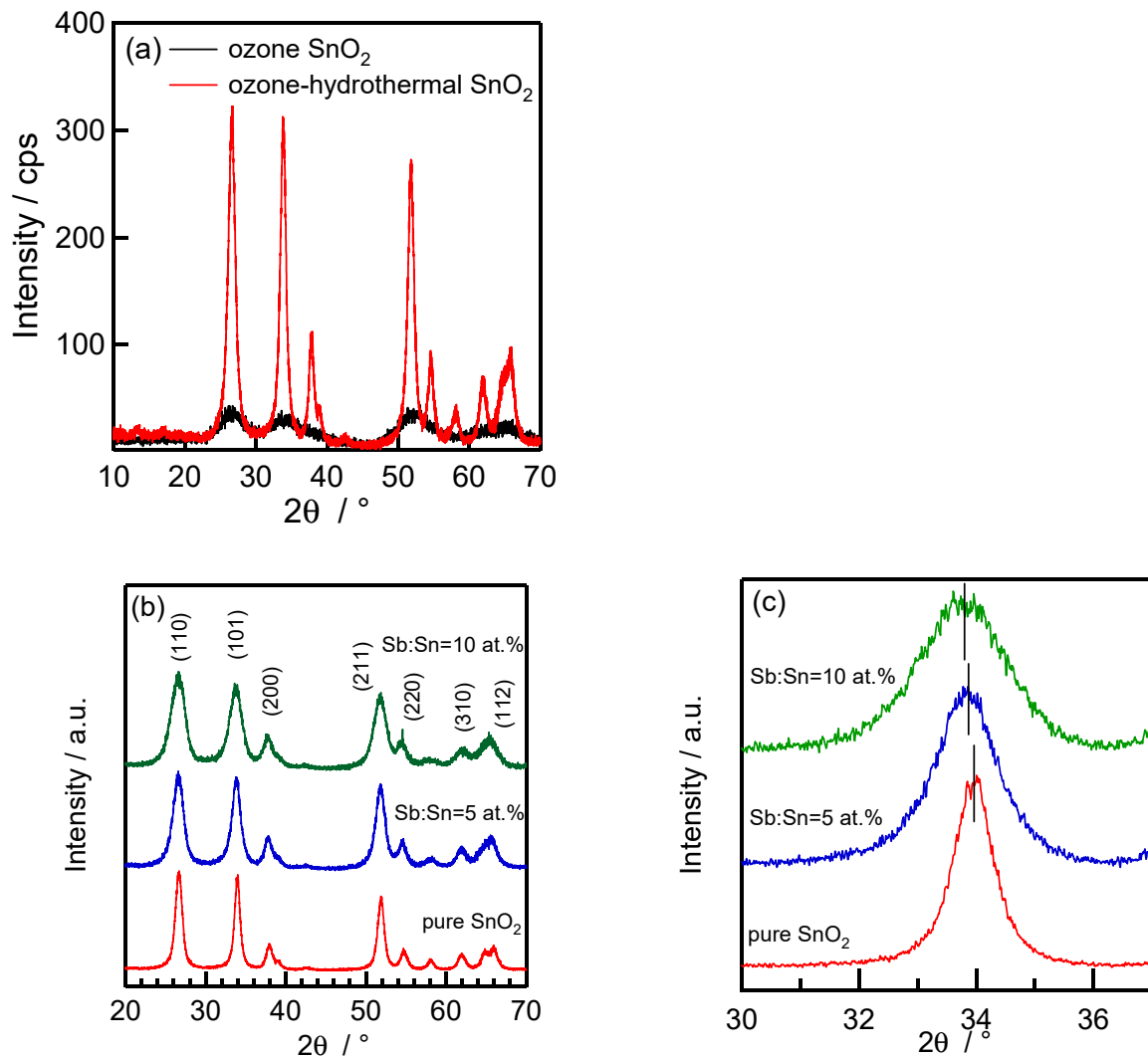


**Figure 2.** X-ray diffraction (XRD) spectra of  $\text{SnO}_2$  and  $\text{Sb-SnO}_2$ : (a) ozone-assisted process [51] and ozone-assisted hydrothermal process, (b)  $\text{Sb-SnO}_2$  with different antimony concentration ( $\text{Sb/Sn} = 0, 5, 10$  at.%), and (c) enlarged view of (101) in Figure 2b.

As the doping concentration was increased from 0, 5, and 10 at.%, the peak became broader and the full width at half maximum (FWHM) widened, and the crystallite size calculated by Scherrer's equation decreased (Table 2). It has been previously reported that Sb doping decreases the  $\text{SnO}_2$  crystallite size [56], which is generally consistent with the results of the present measurements.

**Table 2.** Crystal and average particle sizes of ozone-assisted SnO<sub>2</sub> with/without hydrothermal treatment with different Sb concentrations. The “crystal/shape size ratio” shows the value of (crystallite size from XRD [nm])/(average particle size from TEM [nm]).

Sb Synthesizing Concentration (at.%)	Crystallite Size from XRD/nm	Average Particle Size from TEM/nm	Crystal/Shape Size Ratio
Ozone SnO <sub>2</sub>	1.44	3.99	0.361
Ozone-hydrothermal SnO <sub>2</sub>	8.56	11.19	0.765
Ozone-hydrothermal 5 at.%-Sb-SnO <sub>2</sub>	5.86	6.63	0.884
Ozone-hydrothermal 10 at.%-Sb-SnO <sub>2</sub>	4.30	4.85	0.887

Figure 3 shows the TEM images of SnO<sub>2</sub> nanoparticles with/without Sb doping. The average particle sizes were summarized in Table 2, compared with the crystal sizes obtained by XRD data (using Scherrer’s equation). The “crystal/shape-sizes ratio (= (crystallite size from XRD [nm]) / (average particle size from TEM [nm]))” was shown. The higher crystal/shape-sizes ratio means higher crystallinity. On the contrary, the lower crystal/shape-sizes ratio means lower crystallinity with an amorphous phase. The SnO<sub>2</sub> by ozone-assisted method is a few nm particles with poor crystallinity (Figure 3a). The average particle size, crystal size, and crystal/shape size ratio were 3.99 nm, 1.44 nm, and 0.361, respectively. These results mean that the ozone-assisted SnO<sub>2</sub> has lower crystallinity with a thick amorphous phase as the shell. In contrast, it can be confirmed that the SnO<sub>2</sub> nanoparticle by ozone-hydrothermal method shows high crystallinity with 11.19 nm of the average particle size (Figure 3b), 8.56 nm of the crystal size, and 0.765 of the crystal/shape size ratio, which is due to the hydrothermal treatment after the ozone peptization method. Also, the SnO<sub>2</sub> nanoparticle has a very angular shape, and the crystalline surface can be clearly seen. Figure 3c,d are TEM images of 5 and 10 at.% of Sb-doped SnO<sub>2</sub> by ozone-assisted hydrothermal method, respectively. As with pure SnO<sub>2</sub>, the presence of nanoparticles with high crystallinity can be confirmed because of the high value of the crystal/shape size ratio (>0.88). The particle size decreases with increasing doping concentration (Table 2), which corresponds to the crystallite size calculated from XRD.

Figure 4a shows the results of the survey scan of XPS. For both SnO<sub>2</sub> and 5 at.% Sb-SnO<sub>2</sub> samples, the distinct peaks for Sn and O were detected. The magnified views of O1s and Sb 3d<sub>3/2</sub> and of Sn 4d were shown in Figure 4b,c, respectively. In Figure 4b, the peak of Sb 3d<sub>3/2</sub> was detected, and the O1s peak of 5 at.% Sb-SnO<sub>2</sub> is slightly broadened compared to the peak of SnO<sub>2</sub>, which is due to the increasing energy distribution in the oxygen atom. Moreover, in Figure 4c, the Sn 4d peak of 5 at.% Sb-SnO<sub>2</sub> also widened the binding energy compared to the peak of SnO<sub>2</sub>. By the above results of XRF, XRD, and XPS measurements, it was confirmed that the Sb is appropriately doped in the SnO<sub>2</sub> lattice with the expansion and squeezing of the SnO<sub>2</sub> lattice.

To observe the dispersing condition of nanoparticles in solution, dynamic light scattering (DLS) measurements were performed in water (Figure 5). The average particle sizes calculated from the DLS measurement were 106.5 nm and 87.5 nm for pure SnO<sub>2</sub> and 5 at.% Sb-SnO<sub>2</sub>, respectively. Since the average crystallite size of SnO<sub>2</sub> was 11.19 nm by TEM results, SnO<sub>2</sub> exists as an aggregate of approximately nine particles in diameter in an aqueous solution. The average aggregate of 5 at.% Sb-SnO<sub>2</sub> nanoparticle was smaller than that of SnO<sub>2</sub>. This may be due to the smaller nanoparticle size of 5 at.% Sb-SnO<sub>2</sub> than that of pure SnO<sub>2</sub>. Hence, there is no variation by Sb doping about the dispersibility.

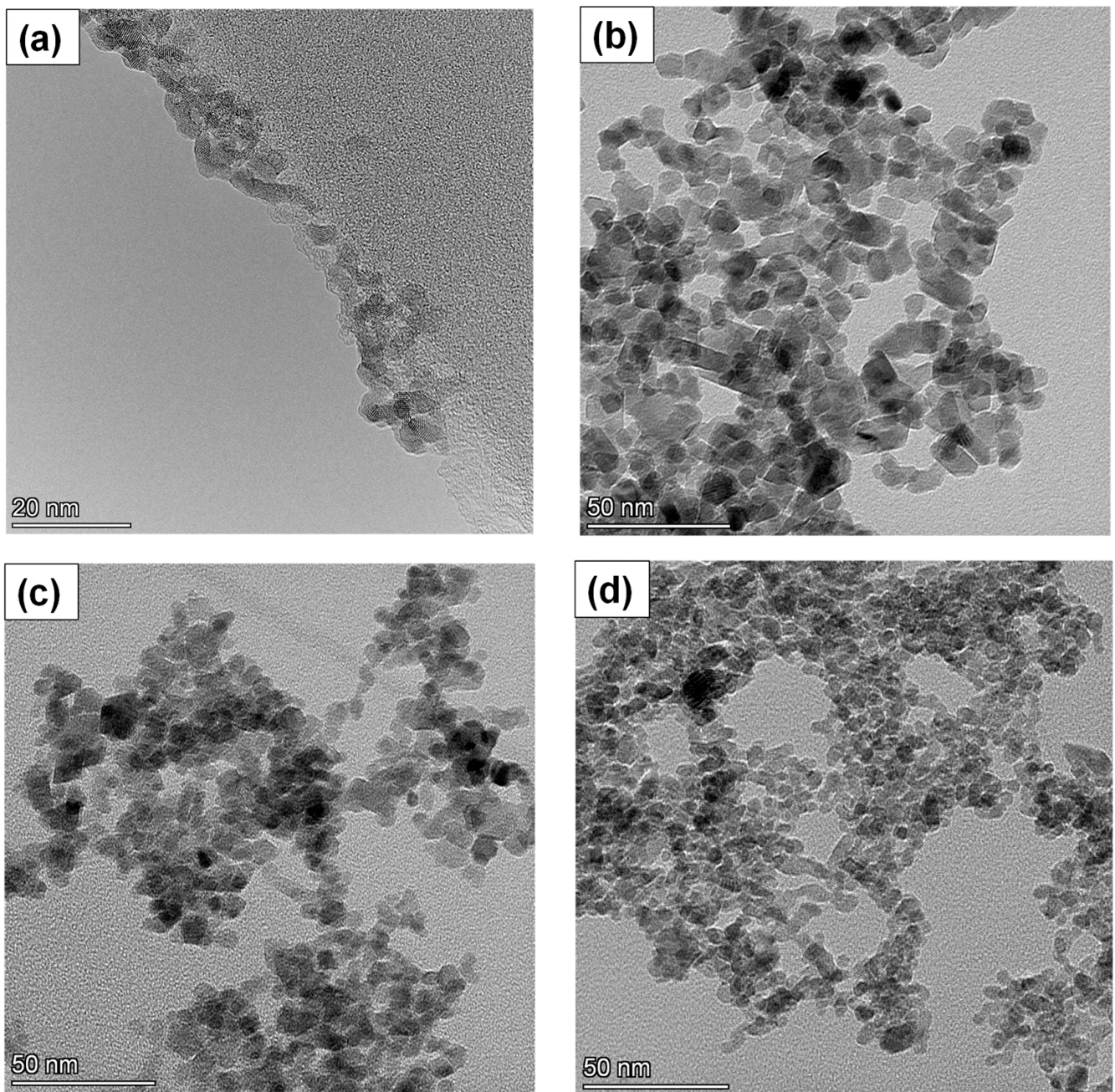


**Figure 3.** TEM images of SnO<sub>2</sub>: (a) pure SnO<sub>2</sub> synthesizing by ozone-assisted method, (b) pure SnO<sub>2</sub> synthesizing by ozone-assisted hydrothermal method, (c) 5 at.% Sb-doped SnO<sub>2</sub> synthesizing by ozone-assisted hydrothermal method, and (d) 10 at.% Sb-doped SnO<sub>2</sub> synthesizing by ozone-assisted hydrothermal method.



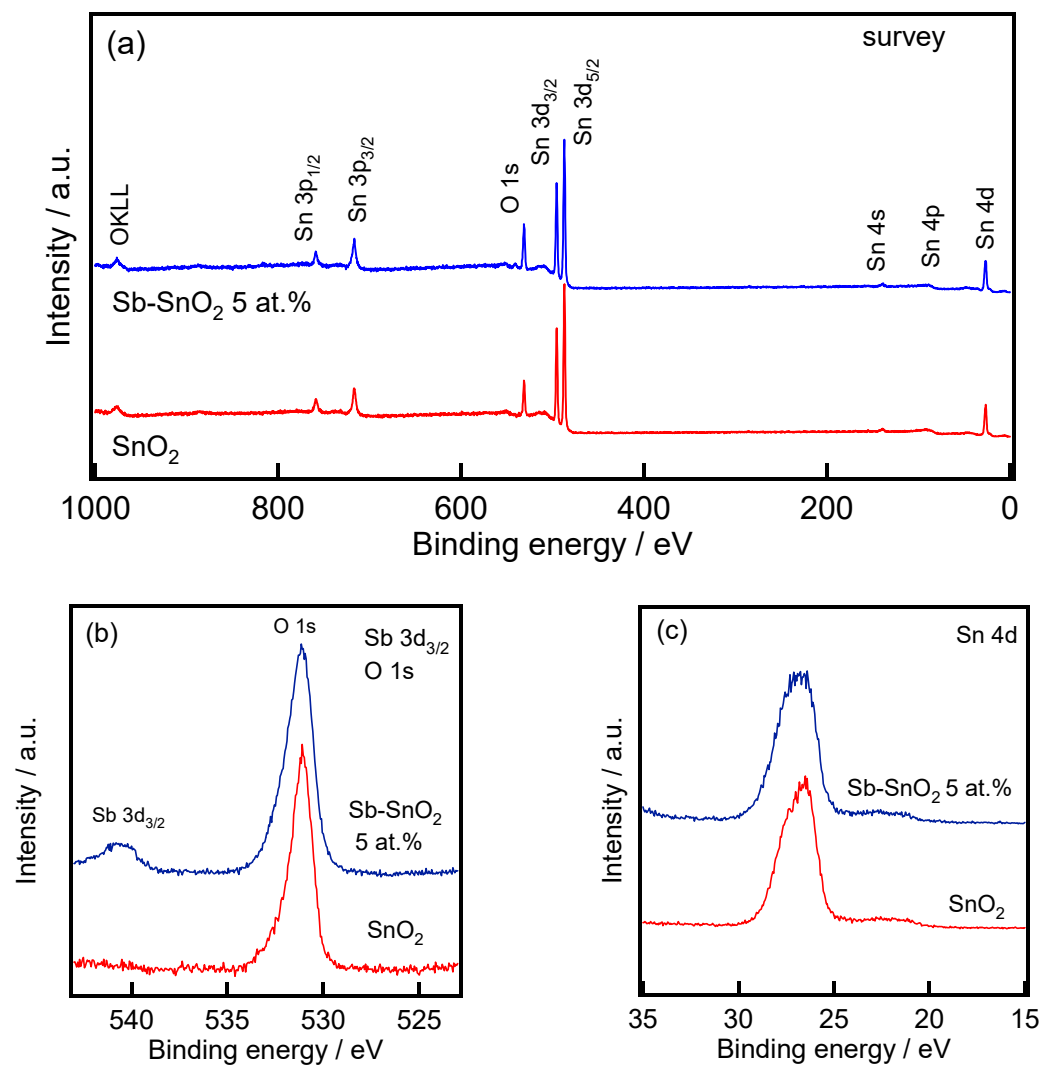


**Figure 4.** X-ray photoelectron spectroscopy (XPS) spectra of pure SnO<sub>2</sub> and 5 at.% Sb-SnO<sub>2</sub>: (a) survey spectra, (b) O1s and Sb 3d spectra, and (c) Sn 4d spectra.

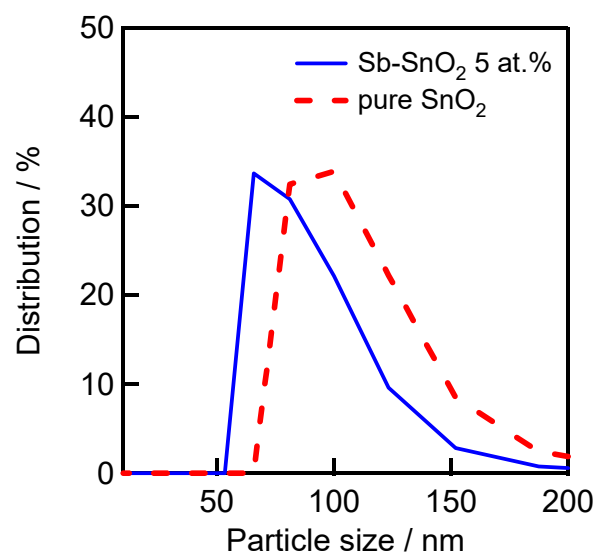


**Figure 5.** Dynamic light scattering (DLS) size distribution plot of pure SnO<sub>2</sub> and 5 at.% Sb-SnO<sub>2</sub>.

Conductivities of the SnO<sub>2</sub> films, 5 at.% Sb-SnO<sub>2</sub>, and 10 at.% Sb-SnO<sub>2</sub> were measured and prepared by spin-coating and annealing on glass substrates. Table 3 shows the sheet resistance, film thickness, and conductivity of each film. The sheet resistance of the SnO<sub>2</sub> was more than 10<sup>7</sup> Ω sq<sup>-1</sup> (over the range of the measurement system). Although the accurate value could not be obtained, it can be said that the pure SnO<sub>2</sub> was an insulating material. In contrast, 5 at.% Sb-SnO<sub>2</sub> had a sheet resistance of 4.03 ± 2.8 × 10<sup>4</sup> Ω sq<sup>-1</sup> and a conductivity of 0.25 S cm<sup>-1</sup>. Hence, the doping of Sb significantly improves conductivity. On the other hand, the excess addition of Sb to “10 at.% Sb-SnO<sub>2</sub>” depressed the conductivity to 0.11 S cm<sup>-1</sup>. So, it was confirmed that excessive Sb doping could be a hindrance to carrier conduction.

**Table 3.** Sheet resistance, film thickness, and conductivity of SnO<sub>2</sub>, 5 at.% Sb-SnO<sub>2</sub>, and 10 at.% Sb-SnO<sub>2</sub>.

Sb Synthesizing Concentration (at.%)	Sb Concentration by XRF (at.%)	Sheet Resistance (Ω·sq <sup>-1</sup> )	Film Thickness (nm)	Conductivity (S·cm <sup>-1</sup> )
0	-	>10 <sup>7</sup> (over range)	939 ± 54	-
5	5.01	4.03 ± 2.8 × 10 <sup>4</sup>	1150 ± 231	0.25 ± 0.12
10	7.94	1.68 ± 0.8 × 10 <sup>5</sup>	950 ± 31	0.11 ± 0.05

UV/VIS measurements were performed on the thin films of SnO<sub>2</sub>, 5 at.% Sb-SnO<sub>2</sub>, and 10 at.% Sb-SnO<sub>2</sub>. Figure 6 shows the absorbance (*y*-axis) of the thin films with the plot on energy (*x*-axis). Each layer has a band gap of around 3.9 eV. Focus on the infrared region (<1 eV), absorption zones were observed in the Sb-SnO<sub>2</sub> films. This shows the formation of donor levels in Sb-SnO<sub>2</sub> thin films due to the Sb doping. Thus, it was confirmed that the enhanced conductivity of the Sb-SnO<sub>2</sub> is due to the formation of donor levels.

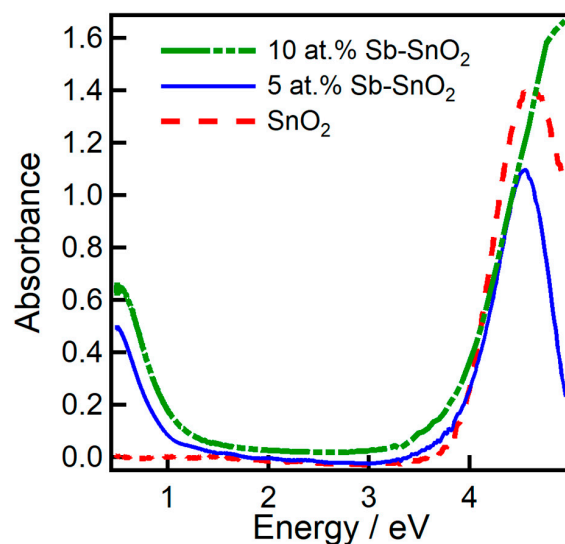


**Figure 6.** Absorption spectra of SnO<sub>2</sub>, 5 at.% Sb-SnO<sub>2</sub>, and 10 at.% Sb-SnO<sub>2</sub>.

### 3.2. Electrochemical Characteristics of Pt/SnO<sub>2</sub> and Pt/Sb-SnO<sub>2</sub>

For the application of the Sb-SnO<sub>2</sub> nanoparticles synthesized via this ozone-assisted hydrothermal method, we have measured the Pt-catalyst-supporting ability using RDE for proton-exchange-membrane fuel cell (PEMFC) as “carbon-support-free PEMFC”. For the Pt/Sb-SnO<sub>2</sub>, the sample of 5 at.% Sb-SnO<sub>2</sub> was used because of better conductivity than 10 at.% Sb-SnO<sub>2</sub>. Hence, instead of writing the catalyst as “Pt/5 at.% Sb-SnO<sub>2</sub>”, it will be written as “Pt/Sb-SnO<sub>2</sub>” in short, below. The PEMFC abilities of prepared Pt/SnO<sub>2</sub> and Pt/Sb-SnO<sub>2</sub> were evaluated by comparison with the commercial Pt/C (TEC10E50E, TANAKA Precious Metals).

Cyclic voltammetry (CV) results for the fabricated Pt/Sb-SnO<sub>2</sub> catalyst are shown in Figure 7a. Both Pt/SnO<sub>2</sub> and Pt/Sb-SnO<sub>2</sub> showed similar voltammograms as Pt/C derived from Pt peaks. A peculiar peak was detected in Pt/Sb-SnO<sub>2</sub> around 0.65 V (not in the CV curve of Pt/C and Pt/SnO<sub>2</sub>). As the first possibility, it can be thought that the 0.65 V peak is attributed to the oxidation of dissolved Sb atom on Pt [44,47]. However, in the literature, the oxidation peaks of Sb and Sn can be observed at 0.47–0.48 V and 0.61–0.8 V, respectively [24,26]. Hence, as the second possibility, it is thought that the 0.65 V peak is due to Sn oxidation, which can be enhanced by the addition of Sb doping in the SnO<sub>2</sub> lattice. The details of the phenomena will be discussed in our future paper, along with the results of XPS, TEM, and additional electrochemical results, considering the effects of strong metal-support interaction (SMSI) [19,28,57,58]. The electrochemical surface area (ECSA) value calculated from the CVs (Figure 7a) is shown in Figure 7b. ECSA was 82.3, 60.3, and 61.7 m<sup>2</sup>g<sup>-1</sup><sub>Pt</sub> for Pt/C, Pt/SnO<sub>2</sub>, and Pt/Sb-SnO<sub>2</sub>, respectively. Hence, the ECSA of Pt on carbon (Pt/C) was better than that on SnO<sub>2</sub> and Sb-SnO<sub>2</sub>.

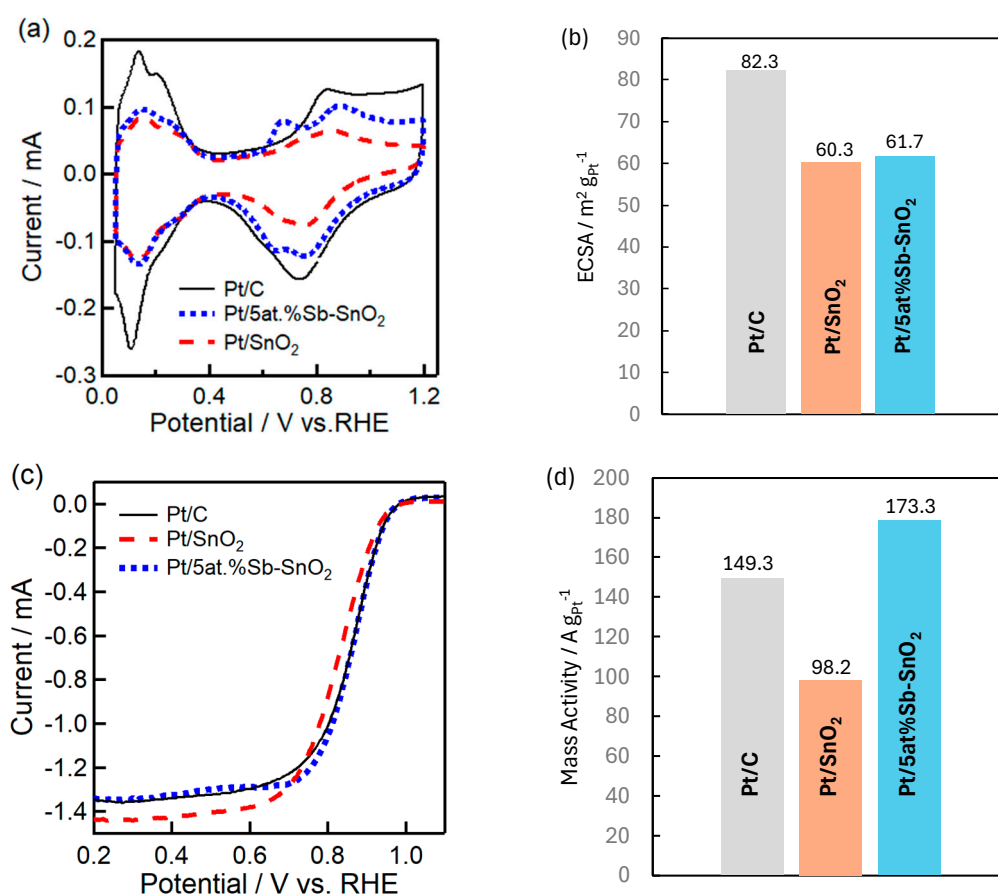
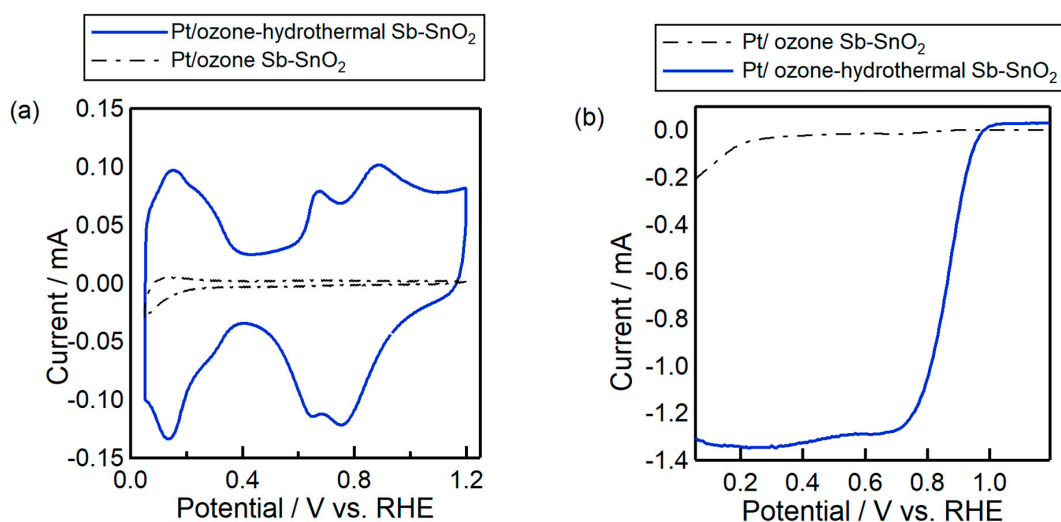


**Figure 7.** Electrochemical measurements of commercial Pt/C, Pt/SnO<sub>2</sub>, and Pt/5 at.% Sb-SnO<sub>2</sub> catalysts using RDE: (a) cyclic voltammograms with N<sub>2</sub> saturation (rotation speed at 0 rpm), (b) ECSA calculated from Figure 7a, (c) linear sweep voltammograms with O<sub>2</sub> saturation (rotation speed at 2500 rpm), and (d) MA calculated from Figure 7c.

Figure 7c,d show the results of LSV and the resulting oxygen reduction reaction (ORR) activity. The onset potential of Pt/Sb-SnO<sub>2</sub> is located on the slightly higher voltage side compared to Pt/C and Pt/SnO<sub>2</sub>. This shows that the ORR activity is enhanced by Sb doping. The mass activity was 149.3, 98.2, and 173.3 A g<sub>Pt</sub><sup>-1</sup> for Pt/C, Pt/SnO<sub>2</sub>, and Pt/Sb-SnO<sub>2</sub>, respectively. The Pt/Sb-SnO<sub>2</sub> recorded the highest mass activity in this work, which would be due to the high conductivity of Sb-SnO<sub>2</sub> and SMSI of Pt/Sb-SnO<sub>2</sub>. This MA value of Pt/Sb-SnO<sub>2</sub> (173.3 A g<sub>Pt</sub><sup>-1</sup>) is one of the highest results in published Sb-SnO<sub>2</sub>. In Pt/SnO<sub>2</sub> catalysts, on the contrary, the lower conductivity of pure SnO<sub>2</sub> results in lower

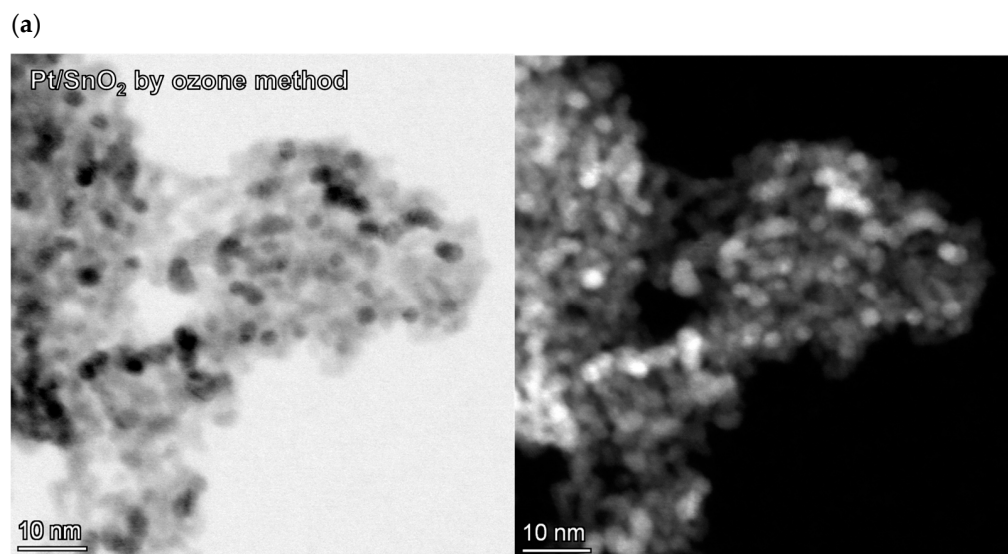
mass activity. However, since the LSV curve of Pt/SnO<sub>2</sub> shows a high current close to Pt/C and Pt/Sb-SnO<sub>2</sub>. Hence, Pt/SnO<sub>2</sub> is also promising for the PEMFC catalyst.

Figure 8 is the comparison of Pt/Sb-SnO<sub>2</sub> with different synthesizing methods (ozone and ozone-hydrothermal methods, shown in Figure 1). The catalysts without hydrothermal treatment exhibited lower catalytic performance. On the other hand, in the CV measurements (Figure 8a), the catalysts with hydrothermal treatment showed clear Pt peaks. In the LSV (Figure 8b), the hydrothermal-treated catalyst performed a high current below 0.9 V for the oxygen reduction reaction.



**Figure 8.** Electrochemical measurements of Pt/Sb-SnO<sub>2</sub> catalyst activity with different synthesizing methods using RDE of (a) cyclic voltammograms with N<sub>2</sub> saturation (rotation speed at 0 rpm) and (b) linear sweep voltammograms with O<sub>2</sub> saturation (rotation speed at 2500 rpm).

In order to discuss the catalytic activity, TEM observations were performed. Figure 9 shows STEM/High angle annular dark-field (HAADF) STEM images of Pt/SnO<sub>2</sub> and Pt/Sb-SnO<sub>2</sub>. In HAADF-STEM images, the white parts show the position of Pt nanoparticles on SnO<sub>2</sub> and/or Sb-SnO<sub>2</sub>. Without the hydrothermal method (Pt/ozone SnO<sub>2</sub> in Figure 9a and Pt/ozone Sb-SnO<sub>2</sub> in Figure 9b), the size of Pt nanoparticles was not so homogeneous (large and small particles), and each Pt nanoparticles were not so much connected.



**Figure 9.** Cont.

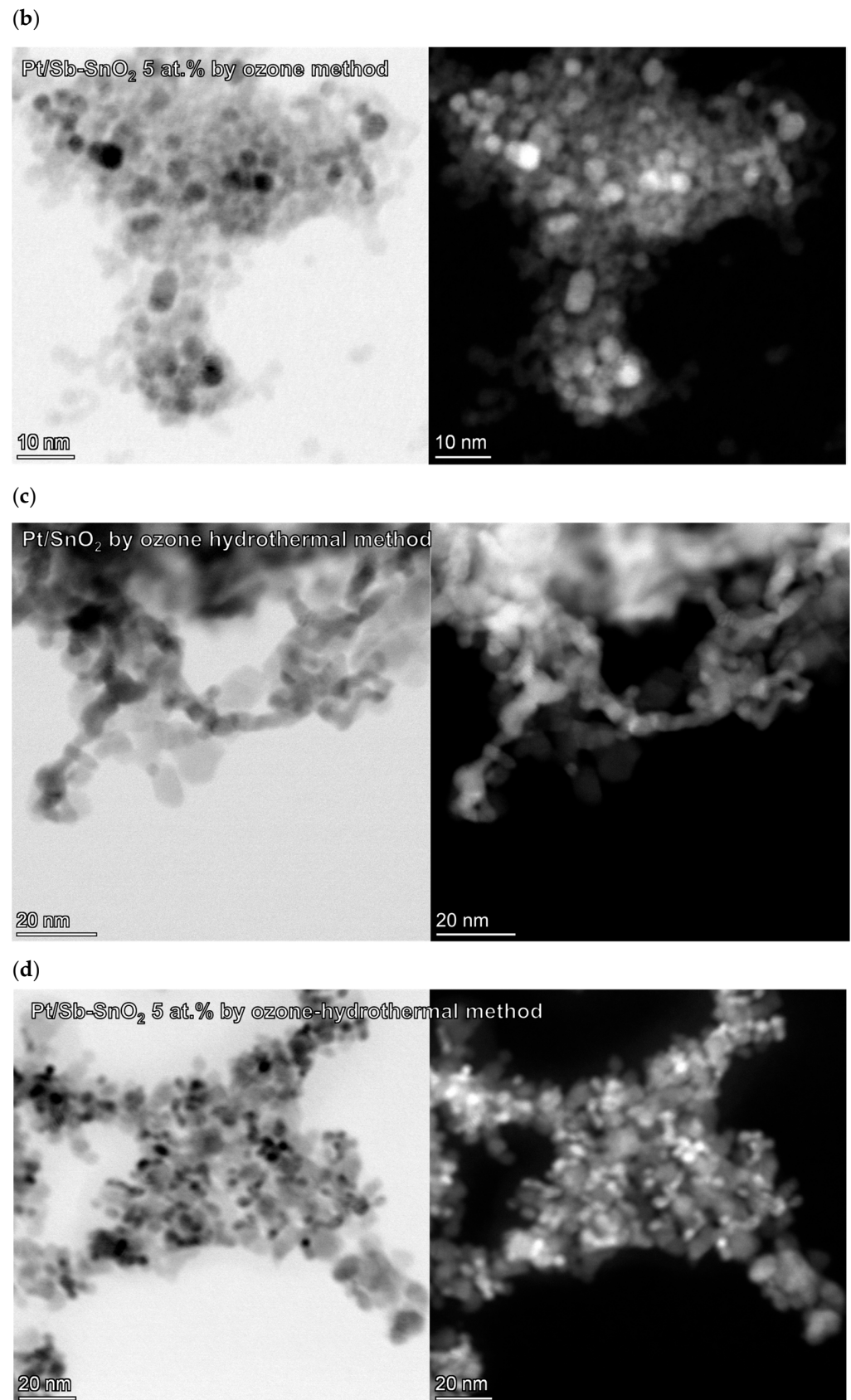


**Figure 9.** STEM and HAADF-STEM images of Pt/SnO<sub>2</sub> and Pt/5 at.% Sb-SnO<sub>2</sub> with different synthesizing method: (a) Pt/SnO<sub>2</sub> by ozone method, (b) Pt/5 at.% Sb-SnO<sub>2</sub> by ozone method, (c) Pt/SnO<sub>2</sub> by ozone-hydrothermal method, and (d) Pt/5 at.% Sb-SnO<sub>2</sub> by ozone-hydrothermal method.

With the ozone-assisted hydrothermal method without Sb doping (Pt/ozone-hydrothermal SnO<sub>2</sub> in Figure 9c), the Pt nanoparticles were significantly connected to each other on the SnO<sub>2</sub> surface. This Pt network may be formed due to the redox reaction from H<sub>2</sub>PtCl<sub>6</sub> to Pt nanoparticles on the surface of the SnO<sub>2</sub> crystal. The Pt nanoparticles network on the crystal surface of ozone-hydrothermal SnO<sub>2</sub> may enhance the ORR.

With the Sb-doping and ozone-assisted hydrothermal method (Pt/ozone-hydrothermal Sb-SnO<sub>2</sub> in Figure 9d), the small Pt nanoparticles were dispersed on the SnO<sub>2</sub> surface and a bit connected to each other. The conducting ozone-hydrothermal Sb-SnO<sub>2</sub> shows high ORR activity with small Pt nanoparticles forming small aggregation (in Figure 9d).

Figure 10 summarizes the images of catalysts in this work. In Figure 10a, the surface of ozone (Sb-)SnO<sub>2</sub> particles is an amorphous phase (not crystal). Pt nanoparticles were not deposited without connecting to each other. Moreover, ozone (Sb-)SnO<sub>2</sub> does not have the conductivity. Hence, there is not a good pathway for the electrons from graphite electrodes to the reaction site (the surface of Pt nanoparticles). Contrary, in Figure 10b for ozone-hydrothermal SnO<sub>2</sub>, the Pt nanoparticles made a network as a “nanowire” on the Rutile crystal surface of ozone-hydrothermal SnO<sub>2</sub>. Although the ozone-hydrothermal SnO<sub>2</sub> does not have the conductivity itself, the Pt nanowire can work the pathway for electrons to the surface of Pt nanoparticles for ORR activation [59,60]. On the other hand, in Figure 10c, the ozone-hydrothermal Sb-SnO<sub>2</sub> has conductivity for the pathway for electrons to the surface of Pt nanoparticles for ORR. Hence, without such long Pt connections, Pt/ozone-hydrothermal Sb-SnO<sub>2</sub> can perform the high ORR activity. Due to the conductivity of the ozone-hydrothermal Sb-SnO<sub>2</sub>, it may not be necessary for Pt nanoparticles to connect each other at the Pt nanoparticle formation with the redox reaction (from H<sub>2</sub>PtCl<sub>6</sub> to Pt nanoparticles).

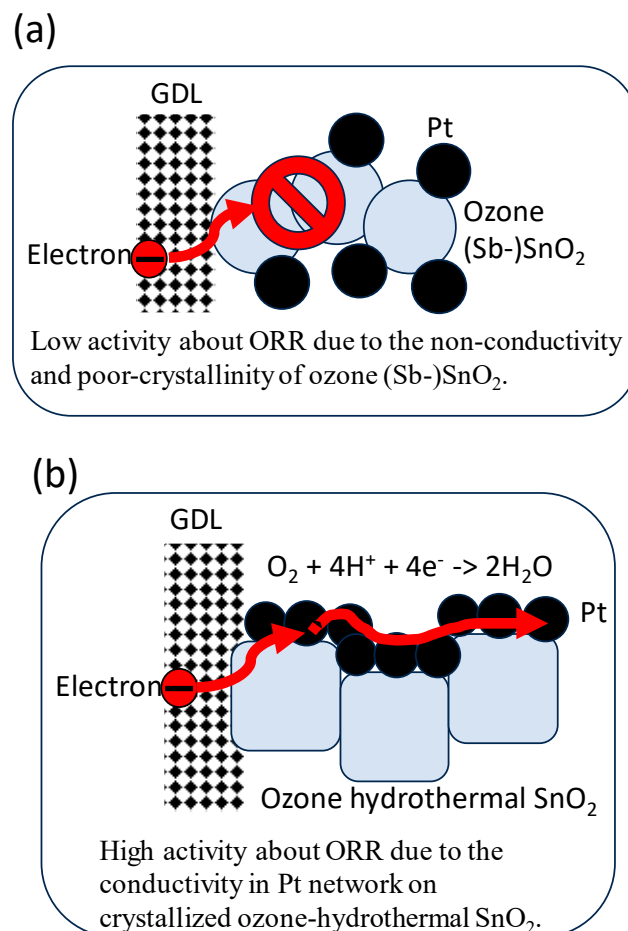
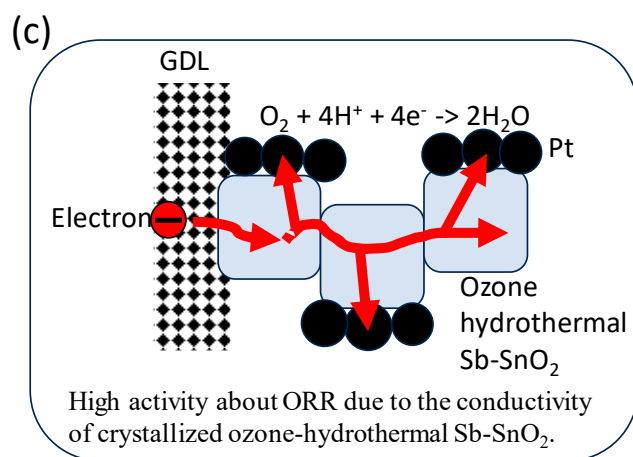


Figure 10. Cont.



**Figure 10.** Working and activation image of catalysts: (a) ozone (Sb-)SnO<sub>2</sub>, (b) ozone-hydrothermal SnO<sub>2</sub>, and (c) ozone-hydrothermal Sb-SnO<sub>2</sub>.

### 3.3. Stability of Pt/SnO<sub>2</sub> and Pt/Sb-SnO<sub>2</sub> as ORR Catalyst

The durability of the catalyst was evaluated using a start-stop protocol. The start-stop protocol is a widely known method for evaluating the durability of catalyst supports in PEMFC [5–7]. At first, the durability of the supporting material (carbon or SnO<sub>2</sub>) was checked by a start-stop protocol (10,000 cycles of voltage sweeping with 0.5 V s<sup>-1</sup> between 1.0 V and 1.5 V) [7] (Figure 11a). Figure 11b shows the transition of ECSA value up to 100,000 cycles, and Figure 11c shows the retention rate of ECSA when the initial value is normalized to 100%. The ECSA retention after 100,000 cycles were 46, 80, and 90% from the initial value of Pt/C, Pt/Sb-SnO<sub>2</sub>, and Pt/SnO<sub>2</sub>, respectively. Pt/SnO<sub>2</sub> and Pt/Sb-SnO<sub>2</sub> showed high durability compared to Pt/C. In Figure 10b, there are crossing points between the ECSA of Pt/C and those of Pt/SnO<sub>2</sub> and Pt/Sb-SnO<sub>2</sub>, around 20,000 cycles. This suggests that Pt/SnO<sub>2</sub> and Pt/Sb-SnO<sub>2</sub> outperform Pt/C in long-term utilization from the viewpoint of application. In order to think about the application probability, we have considered the catalytic stability (CS) against Pt/C.

$$CS = [\text{the final ECSA value of Pt/Sb-SnO}_2] / [\text{the start ECSA value of Pt/C}].$$

If CS can be very good, the catalyst can be considered for commercial application because of the stability issue of Pt/C. The CS values of Pt/SnO<sub>2</sub> and Pt/Sb-SnO<sub>2</sub> at 10,000 cycles were 79.3% and 83.2%, respectively, which are quite high values compared to other publications.

At the second, as another type of durability test, the protocol to accelerate Pt degradation was conducted (in Figure 12a with voltage steps kept at 1.0 V for 3 s and at 0.6 V for 3 s, alternatively [7]). Figure 12b shows the transition of ECSA value up to 100,000 cycles. Since the ESCA of Pt/C in Figure 12 was kept higher than that in Figure 11, there was no crossing point between Pt/C and Pt/(Sb-)SnO<sub>2</sub>, and ECSA of Pt/C was any time better than Pt/(Sb-)SnO<sub>2</sub>. Figure 12c shows the retention rate of ECSA when the initial value is normalized to 100%. The ECSA retention rate of Pt/C, Pt/Sb-SnO<sub>2</sub>, and Pt/SnO<sub>2</sub> after 100,000 cycles were 63, 70, and 81% from the initial value, respectively. Although the catalysts using SnO<sub>2</sub> as a support showed higher durability than Pt/C in Figure 12c, the degradation speed of Pt/Sb-SnO<sub>2</sub> was similar to Pt/C up to 20,000 cycles. So, the Sb-SnO<sub>2</sub> can work on the durability as supporting material (voltage sweeping with 0.5 V s<sup>-1</sup> from 1.0 to 1.5 V), but not so much for Pt durability (voltage steps kept at 1.0 V for 3 s and at 0.6 V for 3 s). The higher durability of Pt/SnO<sub>2</sub> may be due to the platinum linkage structure of Pt/SnO<sub>2</sub> shown in the STEM and HAADF-STEM images. The linked platinum may work to suppress the migration of platinum during operation under degraded conditions like Pt nanowire. Moreover, the SMSI between Pt and SnO<sub>2</sub> supports is also thought to contribute to the realization of high durability. The electronic structure can be changed

by SMSI, which suppresses the migration and desorption of platinum. The details will be published in our future paper.

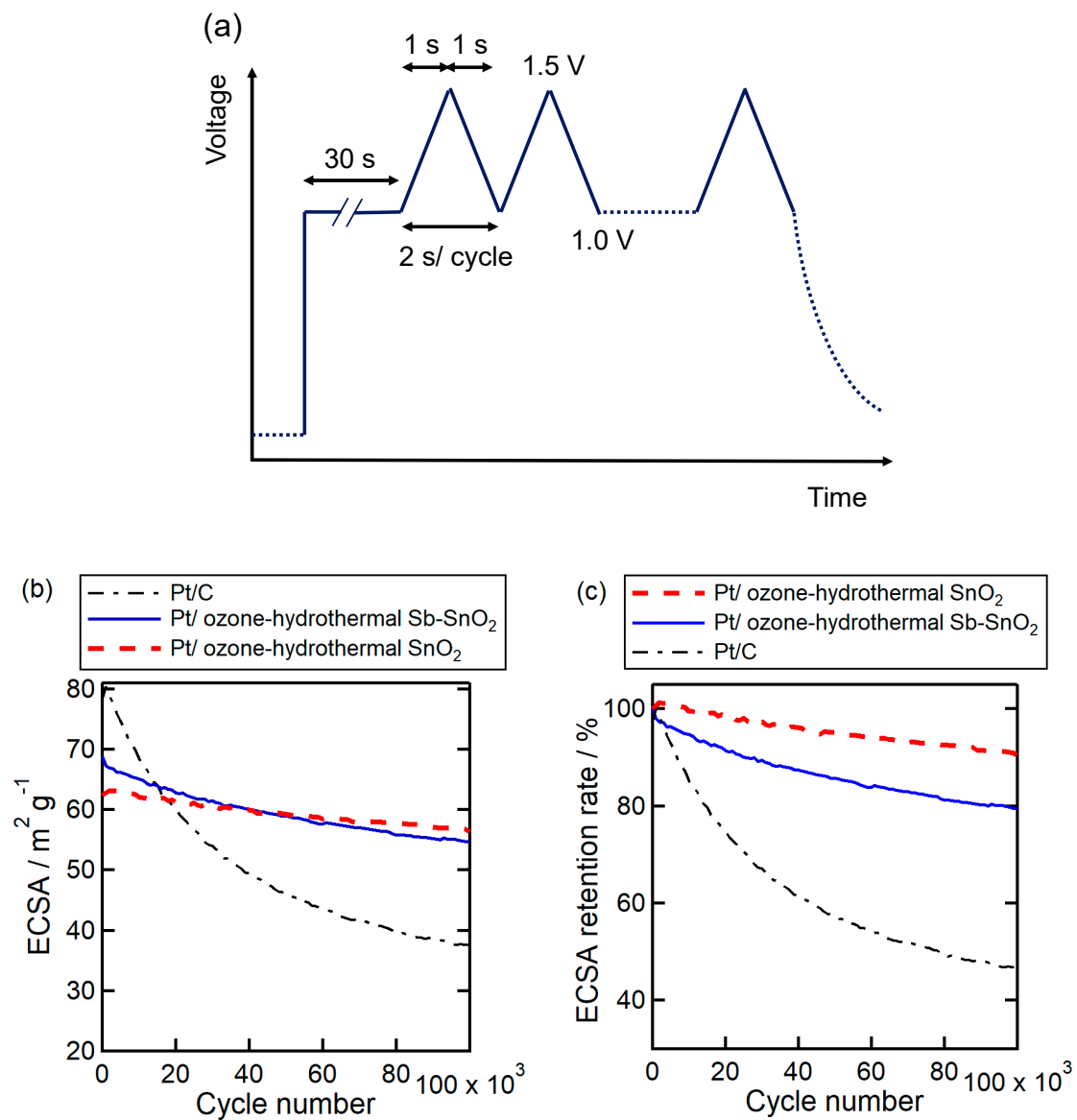


**Figure 11.** Durability of commercial Pt/C, Pt/SnO<sub>2</sub>, and Pt/5 at.% Sb-SnO<sub>2</sub> as a start-stop protocol potential cycles up to 100,000 cycles with voltage sweeping with 0.5 V s<sup>-1</sup> from 1.0 to 1.5 V) to check the durability of supporting material (carbon or SnO<sub>2</sub>) [7]: (a) the applied voltage pattern for the stability test; (b) the transition of ECSA value and (c) ECSA retention rate.



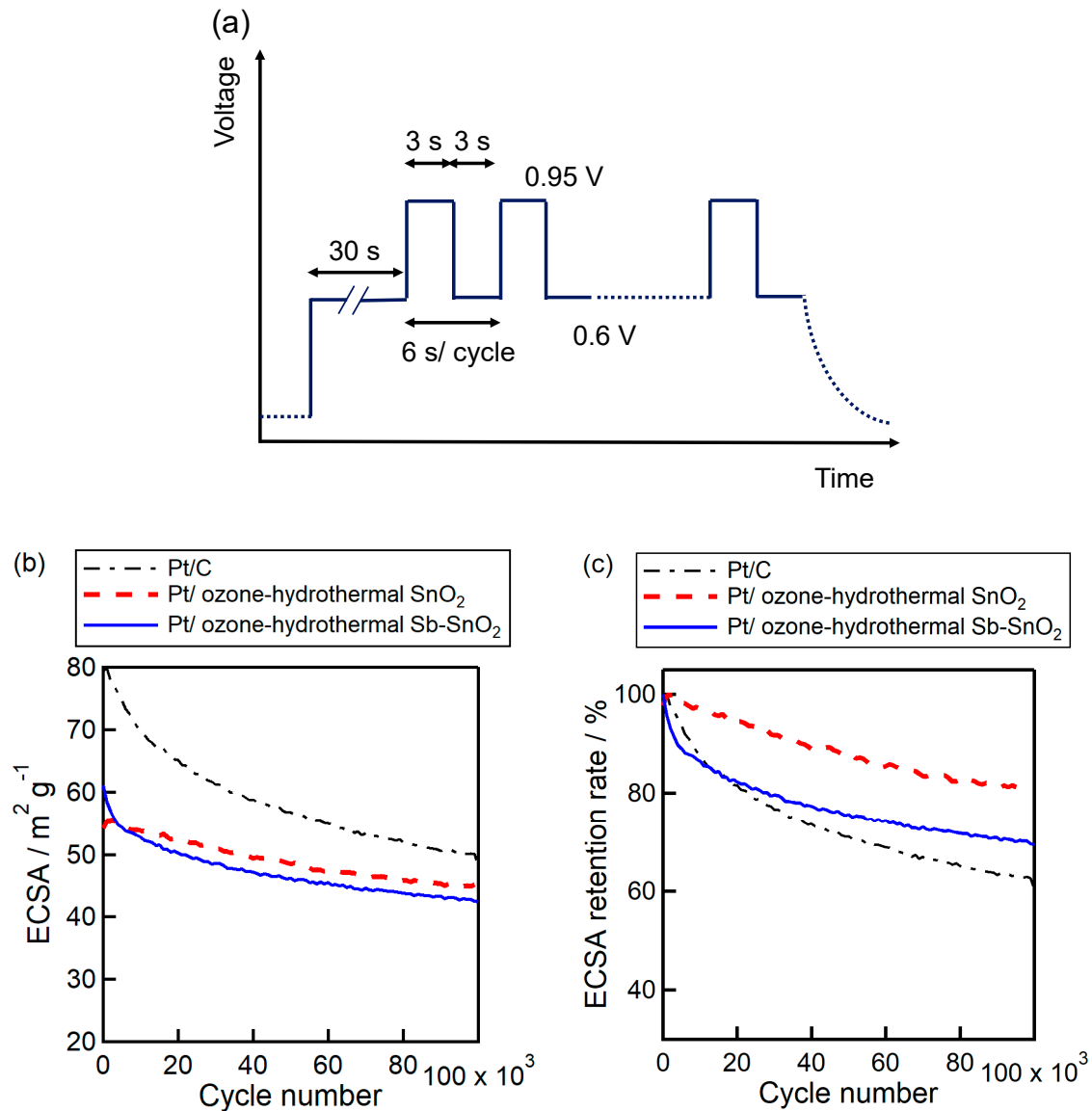


**Figure 12.** Durability of commercial Pt/C, Pt/SnO<sub>2</sub>, and Pt/5 at.% Sb-SnO<sub>2</sub> as an accelerating Pt degradation protocol potential cycles up to 100,000 cycles with voltage steps kept at 1.0 V for 3 s and at 0.6 V for 3 s, alternatively, to check the durability of Pt nanoparticles [7]: (a) the applied voltage pattern for the stability test; (b) the transition of ECSA value and (c) ECSA retention rate.

#### 4. Conclusions

SnO<sub>2</sub>, 5 at.% Sb-SnO<sub>2</sub>, and 10 at.% Sb-SnO<sub>2</sub> were prepared using an ozone-assisted hydrothermal method, which is a simple combination of ozone bubbling and hydrothermal treatment. In XRF, XRD, and XPS results revealed that the Sb is appropriately doped in the SnO<sub>2</sub> lattice at 5 at.% of Sb mixing, but some Sb remained out of the lattice at 10 at.% of Sb mixing. In conductivity of films, 5 at.% Sb-SnO<sub>2</sub> recorded the conductivity of  $0.25 \pm 0.12 \text{ S cm}^{-1}$ , which would be a significant help for the higher MA value ( $178.3 \text{ A g}_{\text{Pt}}^{-1}$ ) than that of Pt/C. The durability of Pt/SnO<sub>2</sub> and Pt/5 at.% Sb-SnO<sub>2</sub> (voltage sweeping with  $0.5 \text{ V s}^{-1}$  from 1.0 to 1.5 V) were much higher than Pt/C and recorded the ECSA retention of 90% and 80% at 100,000 cycles. Therefore, Pt/SnO<sub>2</sub> and Pt/5 at.% Sb-SnO<sub>2</sub> synthesized using this new ozone-hydrothermal method is a promising carbon-free catalyst support for the long-lifetime PEMFC system. The system electricity generation cost from hydrogen fuel cells can be calculated as  $[(\text{catalyst cost} + \text{another device cost}) + (\text{hydrogen cost})] / [(\text{energy conversion efficiency}) \times (\text{lifetime})]$ . If the catalyst and system

can survive forever, the cost of the catalyst and system can be negligible. Hence, although the cost of Pt is quite high at any time, the lifetime of the catalyst is much more important.

In summary, the high catalytic activity can be attributed to three reasons: (1) improved conductivity due to antimony doping [39], (2) the platinum linkage structure (like platinum nanowire [59,60]), and (3) strong metal support interaction (SMSI) between Pt and Sb-doped SnO<sub>2</sub> [19,28,57,58]. We have measured XPS spectra of Pt 4f orbital in the catalysts (Pt/C, Pt/SnO<sub>2</sub>, and Pt/5 at.% Sb-SnO<sub>2</sub>) to discuss the SMSI. However, due to limitations of the paper length and the number of figures, the future paper will be submitted with detailed discussions about SMSI. The origin of the CV peak at 0.65 V will also be discussed in the next paper.

**Author Contributions:** Conceptualization, T.F., T.Y. and S.I.; methodology, T.F. (electrochemistry), T.Y. (hydrothermal), M.T. (Pt deposition), R.T. (dispersion, electrochemistry), K.I. (ozone synthesis), S.N. (XPS) and N.F. (TEM); data curation, T.F.; writing—original draft preparation, T.F.; writing—review and editing, T.F. and S.I.; supervision, S.I.; project administration, S.I.; funding acquisition, S.I. All authors have read and agreed to the published version of the manuscript.

**Funding:** This work has been supported by Himeji City, Hyogo, Japan, funding number: Himesan-shindai R5-3 gou.

**Data Availability Statement:** The original contributions presented in the study are included in the article, further inquiries can be directed to the corresponding author.

**Conflicts of Interest:** The authors declare no conflict of interest.

## References

1. Zhang, T.; Wang, P.; Chen, H.; Pei, P. A Review of Automotive Proton Exchange Membrane Fuel Cell Degradation under Start-Stop Operating Condition. *Appl. Energy* **2018**, *223*, 249–262. [[CrossRef](#)]
2. Dubau, L.; Lopez-Haro, M.; Castanheira, L.; Durst, J.; Chatenet, M.; Bayle-Guillemaud, P.; Guétaz, L.; Caqué, N.; Rossinot, E.; Maillard, F. Probing the Structure, the Composition and the ORR Activity of Pt<sub>3</sub>Co/C Nanocrystallites during a 3422 h PEMFC Ageing Test. *Appl. Catal. B* **2013**, *142–143*, 801–808. [[CrossRef](#)]
3. Wang, L.; Wurster, P.; Gazdzicki, P.; Roussel, M.; Sanchez, D.G.; Guétaz, L.; Jacques, P.A.; Gago, A.S.; Andreas Friedrich, K. Investigation of Activity and Stability of Carbon Supported Oxynitrides with Ultra-Low Pt Concentration as ORR Catalyst for PEM Fuel Cells. *J. Electroanal. Chem.* **2018**, *819*, 312–321. [[CrossRef](#)]
4. Kangasniemi, K.H.; Condit, D.A.; Jarvi, T.D. Characterization of Vulcan Electrochemically Oxidized under Simulated PEM Fuel Cell Conditions. *J. Electrochem. Soc.* **2004**, *151*, E125. [[CrossRef](#)]
5. Gribov, E.N.; Kuznetsov, A.N.; Voropaev, I.N.; Golovin, V.A.; Simonov, P.A.; Romanenko, A.V.; Okunev, A.G. Analysis of the Corrosion Kinetic of Pt/C Catalysts Prepared on Different Carbon Supports Under the “Start-Stop” Cycling. *Electrocatalysis* **2015**, *7*, 159–173. [[CrossRef](#)]
6. Meier, J.C.; Galeano, C.; Katsounaros, I.; Topalov, A.A.; Kostka, A.; Schüth, F.; Mayrhofer, K.J.J. Degradation Mechanisms of Pt/C Fuel Cell Catalysts under Simulated Start-Stop Conditions. *ACS Catal.* **2012**, *2*, 832–843. [[CrossRef](#)]
7. Ohma, A.; Shinohara, K.; Iiyama, A.; Yoshida, T.; Daimaru, A. Membrane and Catalyst Performance Targets for Automotive Fuel Cells by FCCJ Membrane, Catalyst, MEA WG. *ECS Trans.* **2011**, *41*, 775–784.
8. Reiser, C.A.; Bregoli, L.; Patterson, T.W.; Yi, J.S.; Yang, J.D.; Perry, M.L.; Jarvi, T.D. A Reverse-Current Decay Mechanism for Fuel Cells. *Electrochem. Solid-State Lett.* **2005**, *8*, A273–A276. [[CrossRef](#)]
9. Smiljanić, M.; Bele, M.; Moriau, L.J.; Vélez Santa, J.F.; Menart, S.; Šala, M.; Hrnjić, A.; Jovanovič, P.; Ruiz-Zepeda, F.; Gaberšček, M.; et al. Suppressing Platinum Electrocatalyst Degradation via a High-Surface-Area Organic Matrix Support. *ACS Omega* **2022**, *7*, 3540–3548. [[CrossRef](#)] [[PubMed](#)]
10. Jung, S.M.; Yun, S.W.; Kim, J.H.; You, S.H.; Park, J.; Lee, S.; Chang, S.H.; Chae, S.C.; Joo, S.H.; Jung, Y.; et al. Selective Electrocatalysis Imparted by Metal–Insulator Transition for Durability Enhancement of Automotive Fuel Cells. *Nat. Catal.* **2020**, *3*, 639–648. [[CrossRef](#)]
11. Ioroi, T.; Siroma, Z.; Fujiwara, N.; Yamazaki, S.I.; Yasuda, K. Sub-Stoichiometric Titanium Oxide-Supported Platinum Electrocatalyst for Polymer Electrolyte Fuel Cells. *Electrochem. Commun.* **2005**, *7*, 183–188. [[CrossRef](#)]
12. Chiwata, M.; Kakinuma, K.; Wakisaka, M.; Uchida, M.; Deki, S.; Watanabe, M.; Uchida, H. Oxygen Reduction Reaction Activity and Durability of Pt Catalysts Supported on Titanium Carbide. *Catalysts* **2015**, *5*, 966–980. [[CrossRef](#)]
13. Martín, A.J.; Chaparro, A.M. Influence of Operation Parameters on the Response of a PEMFC with Electrodeposited Pt-WO<sub>3</sub> Cathode. *Fuel Cells* **2014**, *14*, 742–749. [[CrossRef](#)]

14. Escalante-García, I.L.; Duron-Torres, S.M.; Cruz, J.C.; Arguello-Hurtado, L.G. Electrochemical Characterization of IrO<sub>2</sub>-Pt and RuO<sub>2</sub>-Pt Mixtures as Bifunctional Electrodes for Unitized Regenerative Fuel Cells. *J. New Mater. Electrochem. Syst.* **2010**, *13*, 227–233.
15. Altamirano-Gutiérrez, A.; Fernández, A.M.; Rodríguez Varela, F.J. Preparation and Characterization of Pt-CeO<sub>2</sub> and Pt-Pd Electrocatalysts for the Oxygen Reduction Reaction in the Absence and Presence of Methanol in Alkaline Medium. *Int. J. Hydrog. Energy* **2013**, *38*, 12657–12666. [[CrossRef](#)]
16. Ganesan, A.; Narayanasamy, M.; Shunmugavel, K. Self-Humidifying Manganese Oxide-Supported Pt Electrocatalysts for Highly-Durable PEM Fuel Cells. *Electrochim. Acta* **2018**, *285*, 47–59. [[CrossRef](#)]
17. Ávila-Vázquez, V.; Galván-Valencia, M.; Ledesma-García, J.; Arriaga, L.G.; Collins-Martínez, V.H.; Guzman-Martinez, C.; Escalante-García, I.L.; Durón-Torres, S.M. Electrochemical performance of a Sb-doped SnO<sub>2</sub> support synthesized by coprecipitation for oxygen reactions. *J. Appl. Electrochem.* **2015**, *45*, 1175–1185. [[CrossRef](#)]
18. Ma, Y.; Cui, B.; He, L.; Tian, K.; Zhang, Z.; Wang, M. A novel support for platinum electrocatalyst based on mesoporous carbon embedded with bimetallic SnTi oxide as a bifunctional electrocatalyst. *J. Electroanal. Chem.* **2019**, *850*, 113435. [[CrossRef](#)]
19. Ozouf, G.; Cognard, G.; Maillard, F.; Chatenet, M.; Guétaz, L.; Heitzmann, M.; Jacques, P.A.; Beauger, C. Sb-Doped SnO<sub>2</sub> Aerogels Based Catalysts for Proton Exchange Membrane Fuel Cells: Pt Deposition Routes, Electrocatalytic Activity and Durability. *J. Electrochem. Soc.* **2018**, *165*, F3036–F3044. [[CrossRef](#)]
20. Kakati, N.; Maiti, J.; Jee, S.H.; Lee, S.H.; Yoon, Y.S. Hydrothermal Synthesis of PtRu on CNT/SnO<sub>2</sub> Composite as Anode Catalyst for Methanol Oxidation Fuel Cell. *J. Alloys Compd.* **2011**, *509*, 5617–5622. [[CrossRef](#)]
21. Tsukatsune, T.; Takabatake, Y.; Noda, Z.; Daio, T.; Zaitzu, A.; Lyth, S.M.; Hayashi, A.; Sasaki, K. Platinum-Decorated Tin Oxide and Niobium-Doped Tin Oxide PEFC Electrocatalysts: Oxygen Reduction Reaction Activity. *J. Electrochem. Soc.* **2014**, *161*, F1208–F1213. [[CrossRef](#)]
22. Ozouf, G.; Cognard, G.; Maillard, F.; Guetaz, L.; Heitzmann, M.; Beauger, C. SnO<sub>2</sub> Aerogels: Towards Performant and Stable PEMFC Catalyst Supports. *ECS Trans.* **2015**, *69*, 1207–1220. [[CrossRef](#)]
23. Dou, M.; Hou, M.; Liang, D.; Lu, W.; Shao, Z.; Yi, B. SnO<sub>2</sub> Nanocluster Supported Pt Catalyst with High Stability for Proton Exchange Membrane Fuel Cells. *Electrochim. Acta* **2013**, *92*, 468–473. [[CrossRef](#)]
24. Cognard, G.; Ozouf, G.; Beauger, C.; Berthomé, G.; Riassetto, D.; Dubau, L.; Chattot, R.; Chatenet, M.; Maillard, F. Benefits and Limitations of Pt Nanoparticles Supported on Highly Porous Antimony-Doped Tin Dioxide Aerogel as Alternative Cathode Material for Proton-Exchange Membrane Fuel Cells. *Appl. Catal. B* **2017**, *201*, 381–390. [[CrossRef](#)]
25. Takasaki, F.; Matsuie, S.; Takabatake, Y.; Noda, Z.; Hayashi, A.; Shiratori, Y.; Ito, K.; Sasaki, K. Carbon-Free Pt Electrocatalysts Supported on SnO<sub>2</sub> for Polymer Electrolyte Fuel Cells: Electrocatalytic Activity and Durability. *J. Electrochem. Soc.* **2011**, *158*, B1270–B1275. [[CrossRef](#)]
26. Cognard, G.; Ozouf, G.; Beauger, C.; Dubau, L.; López-Haro, M.; Chatenet, M.; Maillard, F. Insights into the Stability of Pt Nanoparticles Supported on Antimony-Doped Tin Oxide in Different Potential Ranges. *Electrochim. Acta* **2017**, *245*, 993–1004. [[CrossRef](#)]
27. Fabbri, E.; Rabis, A.; Kötz, R.; Schmidt, T.J. Pt nanoparticles supported on Sb-doped SnO<sub>2</sub> porous structures: Developments and issues. *Phys. Chem. Chem. Phys.* **2014**, *16*, 13672. [[CrossRef](#)] [[PubMed](#)]
28. Spasov, D.D.; Ivanova, N.A.; Pushkarev, A.S.; Pushkareva, I.V.; Presnyakova, N.N.; Chumakov, R.G.; Presnyakov, M.Y.; Grigoriev, S.A.; Fateev, V.N. On the Influence of Composition and Structure of Carbon-Supported Pt-SnO<sub>2</sub> Hetero-Clusters onto Their Electrocatalytic Activity and Durability in PEMFC. *Catalysts* **2019**, *9*, 803. [[CrossRef](#)]
29. Manikandan, M.; Ramesh, G.V.; Tanabe, T.; Dakshnamoorthy, A.; Ariga, K.; Abe, H. Hierarchical SnO<sub>2</sub> Nanostructure with High Energy {113} Facet as Pt-Support for Improved Oxygen Reduction Reaction. *J. Nanosci. Nanotechnol.* **2017**, *17*, 2929. [[CrossRef](#)]
30. Du, C.; Chen, M.; Cao, X.; Yin, G.; Shi, P. A novel CNT@SnO<sub>2</sub> core–sheath nanocomposite as a stabilizing support for catalysts of proton exchange membrane fuel cells. *Electrochem. Commun.* **2009**, *11*, 496–498. [[CrossRef](#)]
31. Yatheendran, A.; Rajan, R.; Sandhyarani, N. Synergistic Effect of Oxygen Vacancy-Rich SnO<sub>2</sub> and AgCl in the Augmentation of Sustained Oxygen Reduction Reaction. *Langmuir* **2023**, *39*, 11708–11719. [[CrossRef](#)]
32. Kakinuma, K.; Uchida, M.; Kamino, T.; Uchida, H.; Watanabe, M. Synthesis and Electrochemical Characterization of Pt Catalyst Supported on Sn<sub>0.96</sub>Sb<sub>0.04</sub>O<sub>2-δ</sub> with a Network Structure. *Electrochim. Acta* **2011**, *56*, 2881–2887. [[CrossRef](#)]
33. Kakinuma, K.; Chino, Y.; Senoo, Y.; Uchida, M.; Kamino, T.; Uchida, H.; Deki, S.; Watanabe, M. Characterization of Pt Catalysts on Nb-Doped and Sb-Doped SnO<sub>2-δ</sub> Support Materials with Aggregated Structure by Rotating Disk Electrode and Fuel Cell Measurements. *Electrochim. Acta* **2013**, *110*, 316–324. [[CrossRef](#)]
34. Shi, G.; Hashimoto, T.; Tryk, D.A.; Tano, T.; Iiyama, A.; Uchida, M.; Kakinuma, K. Enhanced Oxygen Reduction Electrocatalysis on PtCoSn Alloy Nanocatalyst Mediated by Ta-Doped SnO<sub>2</sub> Support for Polymer Electrolyte Fuel Cells. *Electrochim. Acta* **2021**, *390*, 138894. [[CrossRef](#)]
35. Shi, G.; Tano, T.; Tryk, D.A.; Iiyama, A.; Uchida, M.; Kakinuma, K. Temperature Dependence of Oxygen Reduction Activity at Pt/Nb-Doped SnO<sub>2</sub> Catalysts with Varied Pt Loading. *ACS Catal.* **2021**, *11*, 5222–5230. [[CrossRef](#)]

36. Kakinuma, K.; Hayashi, M.; Hashimoto, T.; Iiyama, A.; Uchida, M. Enhancement of the Catalytic Activity and Load Cycle Durability of a PtCo Alloy Cathode Catalyst Supported on Ta-Doped SnO<sub>2</sub> with a Unique Fused Aggregated Network Microstructure for Polymer Electrolyte Fuel Cells. *ACS Appl. Energy Mater.* **2020**, *3*, 6922–6928. [[CrossRef](#)]
37. Kakinuma, K.; Suda, K.; Kobayashi, R.; Tano, T.; Arata, C.; Amemiya, I.; Watanabe, S.; Matsumoto, M.; Imai, H.; Iiyama, A.; et al. Electronic States and Transport Phenomena of Pt Nanoparticle Catalysts Supported on Nb-Doped SnO<sub>2</sub> for Polymer Electrolyte Fuel Cells. *ACS Appl. Mater. Interfaces* **2019**, *11*, 34957–34963. [[CrossRef](#)]
38. Takei, C.; Kobayashi, R.; Mizushita, Y.; Hiramitsu, Y.; Kakinuma, K.; Uchida, M. Platinum Anti-Dissolution Mechanism of Pt/Nb-SnO<sub>2</sub> Cathode Catalyst Layer during Load Cycling in the Presence of Oxygen for Polymer Electrolyte Fuel Cells. *J. Electrochem. Soc.* **2018**, *165*, F1300–F1311. [[CrossRef](#)]
39. Chino, Y.; Kakinuma, K.; Tryk, D.A.; Watanabe, M.; Uchida, M. Influence of Pt Loading and Cell Potential on the HF Ohmic Resistance of an Nb-Doped SnO<sub>2</sub>-Supported Pt Cathode for PEFCs. *J. Electrochem. Soc.* **2016**, *163*, F97–F105. [[CrossRef](#)]
40. Kakinuma, K.; Kobayashi, R.; Iiyama, A.; Uchida, M. Influence of Ionomer Content on Both Cell Performance and Load Cycle Durability for Polymer Electrolyte Fuel Cells Using Pt/Nb-SnO<sub>2</sub> Cathode Catalyst Layers. *J. Electrochem. Soc.* **2018**, *165*, J3083–J3089. [[CrossRef](#)]
41. Chino, Y.; Taniguchi, K.; Senoo, Y.; Kakinuma, K.; Hara, M.; Watanabe, M.; Uchida, M. Effect of Added Graphitized CB on Both Performance and Durability of Pt/Nb-SnO<sub>2</sub> Cathodes for PEFCs. *J. Electrochem. Soc.* **2015**, *162*, F736–F743. [[CrossRef](#)]
42. Senoo, Y.; Taniguchi, K.; Kakinuma, K.; Uchida, M.; Uchida, H.; Deki, S.; Watanabe, M. Cathodic Performance and High Potential Durability of Ta-SnO<sub>2-δ</sub>-Supported Pt Catalysts for PEFC Cathodes. *Electrochem. Commun.* **2015**, *51*, 37–40. [[CrossRef](#)]
43. Senoo, Y.; Kakinuma, K.; Uchida, M.; Uchida, H.; Deki, S.; Watanabe, M. Improvements in Electrical and Electrochemical Properties of Nb-Doped SnO<sub>2-δ</sub> Supports for Fuel Cell Cathodes Due to Aggregation and Pt Loading. *RSC Adv.* **2014**, *4*, 32180–32188. [[CrossRef](#)]
44. Mohamed, R.; Binninger, T.; Kooyman, P.J.; Hoell, A.; Fabbri, E.; Patru, A.; Heinritz, A.; Schmidt, T.J.; Levecque, P. Facile Deposition of Pt Nanoparticles on Sb-Doped SnO<sub>2</sub> Support with Outstanding Active Surface Area for the Oxygen Reduction Reaction. *Catal. Sci. Technol.* **2018**, *8*, 2672–2685. [[CrossRef](#)]
45. Jimenez-Morales, I.; Haidar, F.; Cavaliere, S.; Jones, D.; Roziere, J. Strong Interaction between Platinum Nanoparticles and Tantalum-Doped Tin Oxide Nanofibers and Its Activation and Stabilization Effects for Oxygen Reduction Reaction. *ACS Catal.* **2020**, *10*, 10399–10411. [[CrossRef](#)]
46. Cavaliere, S.; Subianto, S.; Savych, I.; Tillard, M.; Jones, D.; Roziere, J. Dopant-Driven Nanostructured Loose-Tube SnO<sub>2</sub> Architectures: Alternative Electrocatalyst Supports for Proton Exchange Membrane Fuel Cells. *J. Phys. Chem. C* **2013**, *117*, 18298–18307. [[CrossRef](#)]
47. He, C.; Wang, X.; Sankarasubramanian, S.; Yadav, A.; Bhattacharyya, K.; Liang, X.; Ramani, V. Highly Durable and Active Pt/Sb-Doped SnO<sub>2</sub> Oxygen Reduction Reaction Electrocatalysts Produced by Atomic Layer Deposition. *ACS Appl. Energy Mater.* **2020**, *3*, 5774–5783. [[CrossRef](#)]
48. Min, H.; Lee, D.Y.; Kim, J.; Kim, G.; Lee, K.S.; Kim, J.; Paik, M.J.; Kim, Y.K.; Kim, K.S.; Kim, M.G.; et al. Perovskite Solar Cells with Atomically Coherent Interlayers on SnO<sub>2</sub> Electrodes. *Nature* **2021**, *598*, 444–450. [[CrossRef](#)]
49. Isono, T.; Fukuda, T.; Nakagawa, K.; Usui, R.; Satoh, R.; Morinaga, E.; Mihara, Y. Highly Conductive SnO<sub>2</sub> Thin Films for Flat-Panel Displays. *J. Soc. Inf. Disp.* **2007**, *15*, 161. [[CrossRef](#)]
50. Wei, B.Y.; Hsu, M.C.; Su, P.G.; Lin, H.M.; Wu, R.J.; Lai, H.J. A Novel SnO<sub>2</sub> Gas Sensor Doped with Carbon Nanotubes Operating at Room Temperature. *Sens. Actuators B Chem.* **2004**, *101*, 81–89. [[CrossRef](#)]
51. Iimura, K.; Ando, S.; Kikuchi, T.; Fujita, Y.; Satone, H.; Suzuki, M. Synthesis of SnO<sub>2</sub> Quantum Dots via Ozone Assisted Process. *J. Soc. Powder Technol. Jpn.* **2017**, *54*, 609–615. [[CrossRef](#)]
52. Lekshmy, S.S.; Daniel, G.P.; Joy, K. Microstructure and Physical Properties of Sol Gel Derived SnO<sub>2</sub>: Sb Thin Films for Optoelectronic Applications. *Appl. Surf. Sci.* **2013**, *274*, 95–100. [[CrossRef](#)]
53. Peters, K.; Zeller, P.; Stefanic, G.; Skoromets, V.; Němec, H.; Kužel, P.; Fattakhova-Rohlfing, D. Water-Dispersible Small Monodisperse Electrically Conducting Antimony Doped Tin Oxide Nanoparticles. *Chem. Mater.* **2015**, *27*, 1090–1099. [[CrossRef](#)]
54. Orfanidi, A.; Daletou, M.K.; Neophytides, S.G. Preparation and Characterization of Pt on Modified Multi-Wall Carbon Nanotubes to be used as Electrocatalysts for High Temperature Fuel Cell Applications. *Appl. Catal. B* **2011**, *106*, 379–389. [[CrossRef](#)]
55. Nbelayim, P.; Ashida, Y.; Maegawa, K.; Kawamura, G.; Muto, H.; Matsuda, A. Preparation and Characterization of Stable and Active Pt@TiO<sub>2</sub> Core-Shell Nanoparticles as Electrocatalyst for Application in PEMFCs. *ACS Appl. Energy Mater.* **2020**, *3*, 3269–3281. [[CrossRef](#)]
56. Xu, J.M.; Li, L.; Wang, S.; Ding, H.L.; Zhang, Y.X.; Li, G.H. Influence of Sb Doping on the Structural and Optical Properties of Tin Oxide Nanocrystals. *CrystEngCom.* **2013**, *15*, 3296–3300. [[CrossRef](#)]
57. Tauster, S.J.; Fung, S.C.; Garten, R.L. Strong Metal-Support Interactions. Group 8 Noble Metals Supported on TiO<sub>2</sub>. *J. Am. Chem. Soc.* **1978**, *100*, 170–175. [[CrossRef](#)]
58. Smiljanić, M.; Panić, S.; Bele, M.; Ruiz-Zepeda, F.; Pavko, L.; Gašparič, L.; Kokalj, A.; Gaberšček, M.; Hodnik, N. Improving the HER Activity and Stability of Pt Nanoparticles by Titanium Oxynitride Support. *ACS Catal.* **2022**, *12*, 13021–13033. [[CrossRef](#)] [[PubMed](#)]

59. Ma, Y.; Gao, W.; Shan, H.; Chen, W.; Shang, W.; Tao, P.; Song, C.; Addiego, C.; Deng, T.; Pan, X.; et al. Platinum-Based Nanowires as Active Catalysts toward Oxygen Reduction Reaction: In Situ Observation of Surface Diffusion-Assisted, Solid-State Oriented Attachment. *Adv. Mater.* **2017**, *29*, 1703460. [[CrossRef](#)] [[PubMed](#)]
60. Li, M.; Zhao, Z.; Cheng, T.; Fortunelli, A.; Chen, C.-Y.; Yu, R.; Zhang, Q.; Gu, L.; Merinov, B.V.; Lin, Z.; et al. Ultrafine jagged platinum nanowires enable ultrahigh mass activity for the oxygen reduction reaction. *Science* **2016**, *354*, 1414–1419. [[CrossRef](#)]

**Disclaimer/Publisher’s Note:** The statements, opinions and data contained in all publications are solely those of the individual author(s) and contributor(s) and not of MDPI and/or the editor(s). MDPI and/or the editor(s) disclaim responsibility for any injury to people or property resulting from any ideas, methods, instructions or products referred to in the content.